nature communications

Article

https://doi.org/10.1038/s41467-025-58727-0

Dual and plasticity-dependent regulation of cerebello-zona incerta circuits on anxiety-like behaviors

Received: 4 October 2024

Accepted: 27 March 2025

Published online: 08 April 2025

Check for updates

Yue Zhao[1,2,3,9], Jin-Tao Wu[4,9], Jia-Bin Feng[2,9], Xin-Yu Cai[2], Xin-Tai Wang[5], Luxi Wang[2], Wei Xie[6], Yan Gu[7], Jun Liu[1] ✉, Wei Chen[2] ✉, Lin Zhou[2] ✉ & Ying Shen[1,2,8] ✉

Clinical observation has identified cerebellar cognitive affective syndrome, which is characterized by various non-motor dysfunctions such as social disorders and anxiety. Increasing evidence has revealed reciprocal mono-/poly-synaptic connections of cerebello-cerebral circuits, forming the concept of the cerebellar connectome. In this study, we demonstrate that neurons in the cerebellar nuclei (CN) of male mice project to a subset of zona incerta (ZI) neurons through long-range glutamatergic and GABAergic transmissions, both capable of encoding acute stress. Furthermore, activating or inhibiting glutamatergic and GABAergic transmissions in the CN → ZI pathway can positively or negatively regulate anxiety and place preference through presynaptic plasticity-dependent mechanisms, as well as mediate motor-induced alleviation of anxiety. Our data support the close relationship between the cerebellum and emotional processes and suggest that targeting cerebellar outputs may be an effective approach for treating anxiety.

Stress induces short-term adaptive changes, leads to long-term maladaptation, and disrupts an individual's internal balance, thereby increasing the risk of anxiety, depression, and other mental disorders[1]. Current studies on stress and anxiety primarily focus on the forebrain and its associated regions, such as the prefrontal cortex, bed nucleus of the stria terminalis (BNST), amygdala, ventral tegmental area (VTA), and hippocampus, as well as their extensive connections[2–5].

The cerebellum has long been thought to be primarily involved in motor regulation. However, increasing clinical observations have indicated its involvement in emotion and mental disorders, leading to the proposal of cerebellar cognitive affective syndrome (CCAS)[6]. Functional magnetic resonance imaging (fMRI) studies have demonstrated that the activation of the cerebellar cortex is associated with emotional and social processes[7]. Additionally, damage to the cerebellum has been correlated with anxiety and depression[8]. Purkinje cells in the cerebellar cortex modulate the activity of the cerebellar nuclei (CN), which comprise the fastigial nucleus (FN), interposed nucleus (IN), and dentate nucleus (DN), through inhibitory outputs. The CN demonstrates wide projections to the forebrain[9–11], and disturbances in cerebellar development can lead to

[1]Department of Neurology, Institute of Neuroscience, Key Laboratory of Neurogenetics and Channelopathies of Guangdong Province and the Ministry of Education of China, The Second Affiliated Hospital, Guangzhou Medical University, Guangzhou, China. [2]Department of Psychiatry, Sir Run Run Shaw Hospital, Zhejiang University School of Medicine, Hangzhou, China. [3]Liangzhu Laboratory, Zhejiang University Medical Center, MOE Frontier Science Center for Brain and Brain-machine Integration, State Key Laboratory of Brain-machine Intelligence, Zhejiang University, Hangzhou, China. [4]School of Basic Medical Sciences, Hangzhou Normal University, Hangzhou, China. [5]Institute of Life Sciences, College of Life and Environmental Sciences, Hangzhou Normal University, Hangzhou, China. [6]The Key Laboratory of Developmental Genes and Human Disease of the Ministry of Education, School of Life Science and Technology, Southeast University, Nanjing, China. [7]Center of Stem Cell and Regenerative Medicine, Zhejiang University School of Medicine, Hangzhou, China. [8]Key Laboratory for Precision Diagnosis, Treatment, and Clinical Translation of Rare Diseases of Zhejiang Province, Zhejiang University School of Medicine, Hangzhou, China. [9]These authors contributed equally: Yue Zhao, Jin-Tao Wu, Jia-Bin Feng. ✉e-mail: liujun@gzhmu.edu.cn; srrcw@zju.edu.cn; lynchow@zju.edu.cn; yshen@zju.edu.cn

developmental and functional abnormalities within the targeted nuclei[12,13].

The connection between the cerebellum and anxiety-related networks has been proposed[14]. First, CN is associated with the autonomic nervous system regulated by the hypothalamus[15], establishing reciprocal circuits for somatic responses to stress and anxiety[16]. Second, there exist reciprocal projections connecting the vestibular and anxiety systems[17], indicating potential involvement of the cerebellum in emotional regulation. Third, CN neurons project to the parafascicular nucleus of the thalamus, which in turn projects to the amygdala, suggesting that the CN may indirectly modulate amygdala function and anxiety through these circuits[18]. Moreover, a recent study demonstrates a direct circuit from the DN to the amygdala, which facilitates the reduction of anxiety through motor activity[19]. These findings give rise to a question: Can anxiety be treated through neuromodulation at the cerebellum? In fact, cerebellar stimulation has been employed to treat cognitive impairments resulting from Alzheimer's disease and stroke[20,21], and to improve affective functions[22], with considerable convenience and more potent effects. However, such an approach necessitates a greater comprehension of cerebellar outputs implicated in anxiety.

In the present work, we investigate the role of cerebello-zona incerta (ZI) circuit in regulating anxiety. We demonstrate that IN and DN neurons directly project to an unrecognized subset of ZI neurons via long-range glutamatergic and GABAergic transmissions, both of which are capable of encoding acute stress. Additionally, we show that manipulation of glutamatergic and GABAergic transmissions in the CN → ZI pathway is sufficient to positively or negatively regulate anxiety and place preference through presynaptic plasticity-dependent mechanisms, as well as to mediate motor-induced alleviation of anxiety.

Results

CN projects to ZI through glutamatergic and GABAergic transmissions

Using a non-transsynaptic tracer, Kebschull et al. [23] show that the CN neurons send out outputs to ipsilateral and contralateral nuclei in the brain stem, middle brain, the thalamus, and the hypothalamus, including the ZI. However, the organization and property of the CN → ZI pathway are unknown. To characterize the structure of the CN → ZI pathway, we sterotaxically injected the AAV1-hSyn-Cre-EGFP (enhanced green fluorescent protein) virus into the FN, IN, or DN of Ai9 reporter mice, which express red tdTomato fluorescence when Cre is present (Supplementary Fig. 1a). This anterograde and transsynaptic tracer can travel along axons and infect postsynaptic neurons across monosynaptic connections, turning them red. Mouse brains were serially sectioned at 20 μm and registered based on the Allen mouse brain atlas, and neurons within the ZI were identified according to the tdTomato-positive cell body shape. We discovered that there were numerous IN and DN recipient neurons in the ZI, but few ZI neurons received FN projection (Supplementary Fig. 1b–e). Furthermore, the receiving neurons of IN and DN projections were restricted within the bregma levels of −2.00 to −2.80 (Supplementary Fig. 1f–h; also see Supplementary Movies S1 and S2). In view of these findings, we chose not to explore the FN → ZI projection in this study, and utilized 'CN' to represent 'IN' and 'DN'.

To further specify the CN → ZI synaptic connections, we injected AAV2/9-hSyn-FLEX-mGFP-2A-synaptophysin-mRuby, an anterograde and non-transsynaptic tracer, into the CN of *vGluT2*-Cre and *vGat*-Cre mice (Fig. 1a). In *vGluT2*-Cre mice, GFP fluorescence was observed in the starter neurons (bregma −5.90 to −6.40) and their axonal tracts (bregma −2.00 to −2.80), while mRuby fluorescence was detected in glutamatergic axonal terminals within the ZI (Fig. 1b and Supplementary Fig. 2a), due to the expression of mRuby-tagged synaptophysin. Interestingly, we also observed GFP and mRuby signals in GABAergic axonal tracts and terminals within the ZI (bregma −2.00 to −2.80) of *vGat*-Cre mice (Fig. 1c and Supplementary Fig. 2b). In addition, both glutamatergic and GABAergic CN outputs project to the same subregions within the ZI (Supplementary Fig. 3).

To reinforce the anterograde tracing study and characterize cell types of starter and target neurons in the CN → ZI pathway, we utilized retrograde transsynaptic tracing by co-injecting rAAV-DIO-TVA-EGFP and rAAV-DIO-RG, followed by RV-ENVA-ΔG-DsRed into the ZI two weeks later. Subsequently, immunohistochemical staining with anti-SMI32 and anti-GABA antibodies was conducted in the CN (Fig. 1d). Here, SMI32 is a specific marker for glutamatergic neurons in the CN[24]. As a result of mixed infection of rAAV-DIO-TVA-EGFP and RV-ENVA-DsRed, initiating ZI neurons exhibited yellow fluorescent signal in *vGluT2*-Cre mice (Fig. 1e). Meanwhile, CN neurons, as target cells, were labeled by transsynaptic RV-ENVA-DsRed red fluorescent signal (Fig. 1e). Further immunohistostaining revealed that approximately 30% of GABAergic CN neurons (termed CN^{GABA}) projected to glutamatergic ZI neurons (termed ZI-GLU) (Fig. 1f), while nearly all $_{ZI\text{-}GLU}CN$ neurons were immunopositive for GABA but not SMI32 (Fig. 1g). Therefore, these cells are named as $_{ZI\text{-}GLU}CN^{GABA}$ neurons.

Using the same strategy, we discovered that in *vGat*-Cre mice, initiating ZI neurons were also labeled yellow while retrogradely traced CN neurons were labeled red (Fig. 1h). Immunohistochemistry showed that around 28% of glutamatergic CN neurons (termed CN^{GLU}) projected to GABAergic ZI (termed ZI-GABA) neurons in *vGat*-Cre mice (Fig. 1i). Unlike *vGluT2*-Cre mice, almost all these cells ($_{ZI\text{-}GABA}CN^{GLU}$) identified as SMI32 positive (Fig. 1j).

To summarize, our anterograde and retrograde tracings reveal that the CN → ZI circuit contains dual glutamatergic and GABAergic and cross projections ($_{ZI\text{-}GABA}CN^{GLU}$ and $_{ZI\text{-}GLU}CN^{GABA}$). Additionally, anterograde tracing using AAV1-hSyn-Cre-EGFP in Ai9 mice excluded the projection from the ZI to the contralateral CN (Supplementary Fig. 4).

Monosynaptic synapses in CN^{GLU} → ZI and CN^{GABA} → ZI circuits

In order to investigate the transmission properties of CN^{GLU} → ZI and CN^{GABA} → ZI circuits, patch-clamp recordings were conducted in acutely prepared ZI slices from *vGluT2*-Cre;Ai14 and *vGat-Cre*;Ai14 mice, which had been injected with non-transsynaptic AAV2/9-FLEX-oChIEF-tdTomato in the CN (Fig. 2a). This resulted in oChIEF expression at axonal terminals of CN neurons in the ZI. Meanwhile, tdTomato was expressed in ZI-GLU and ZI-GABA neurons in *vGluT2*-Cre;Ai14 and *vGat-Cre*;Ai14 mice, respectively, due to Cre recombinase (Fig. 2a). According to our tracing studies, non-ZI-GLU and non-ZI-GABA neurons are putative downstream neurons of glutamatergic and GABAergic CN projections, respectively.

Upon optogenetic stimulation of CN terminals of *vGluT2*-Cre;Ai14 mice, whole-cell responses were recorded from ZI-GLU and non-ZI-GLU neurons at −70 mV and +40 mV under voltage-clamp configuration. Light stimulation failed to elicit any current from all ZI-GLU neurons (Fig. 2b), indicating that CN^{GLU} axons do not innervate ZI-GLU neurons. In a subset of non-ZI-GLU ($tdTomato^-$) neurons (10 out of 34), light pulse elicited robust excitatory postsynaptic currents (EPSCs), which were blocked by tetrodotoxin (TTX) (Fig. 2c). Subsequent addition of 4AP, a potassium channel blocker known to prolong the duration of evoked depolarization[25], restored synaptic responses in responsive $tdTomato^-$ neurons (Fig. 2c, d). These results indicate a monosynaptic connection between CN^{GLU} neurons and non-ZI-GLU neurons. The non-responsive non-ZI-GLU neurons may lack innervation with CN axons.

To investigate the synaptic properties of CN^{GLU} → ZI pathway, 6,7-dinitroquinoxaline-2,3-dione (DNQX), a blocker of AMPA (α-amino-3-hydroxy-5-methyl-4-isoxazolepropionic acid) and kainate receptors, and AP5, a blocker of NMDA (*N*-methyl-D-aspartate) receptor, were added into the bathing solution. The results showed that EPSCs in

https://doi.org/10.1038/s41467-025-58727-0

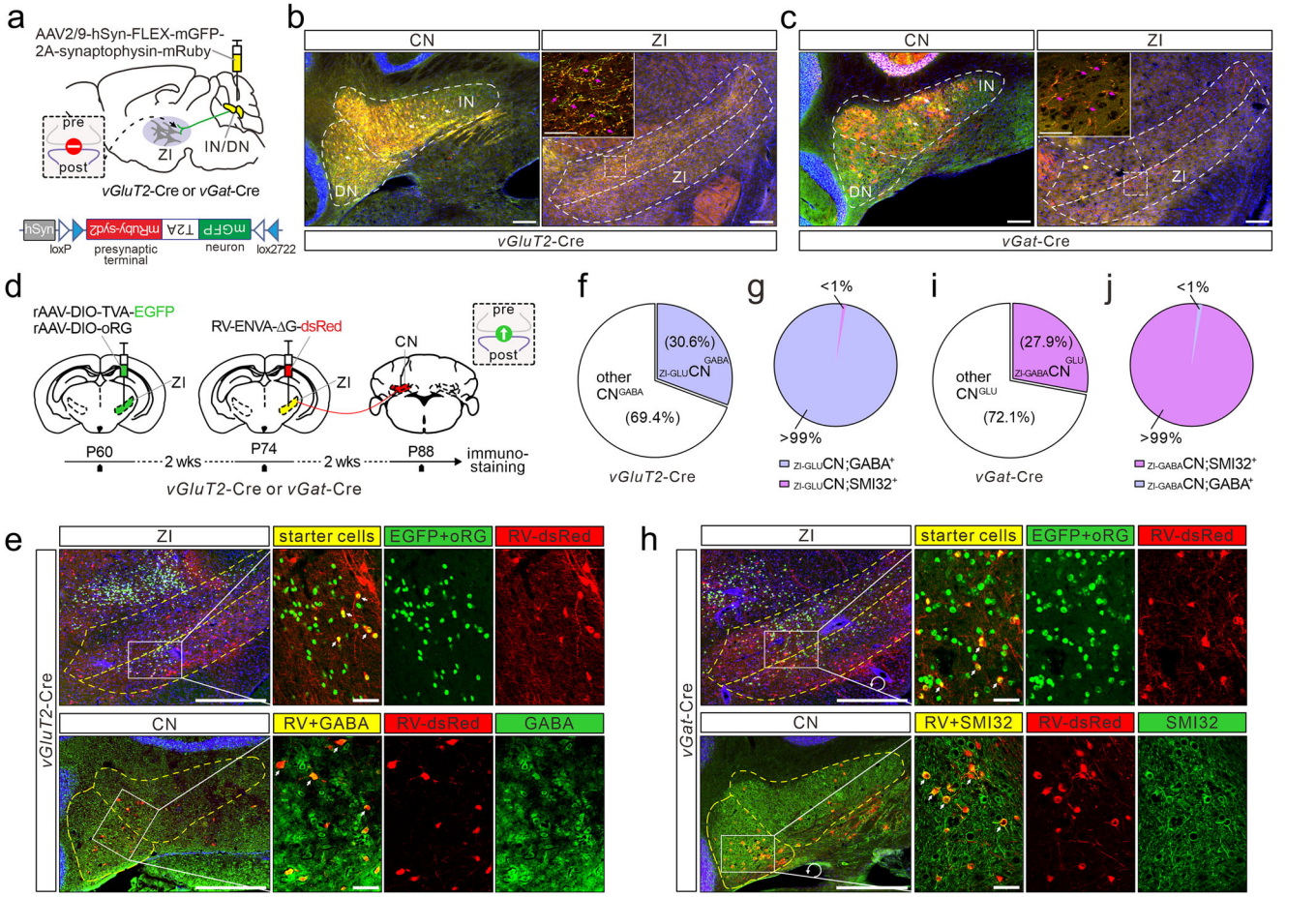

Fig. 1 | Anterograde and retrograde tracings of CN^{GLU} → ZI and CN^{GABA} → ZI circuits. a Schematic illustrating the viral injection and components of the AAV2/9 virus. **b** Left: viral infection (yellow) in CN^{GLU} neurons of *vGluT2*-Cre mice; bregma: −6.20. Right: CN^{GLU} axonal tracts and terminals in contralateral ZI; bregma: −2.50. Scale: 200 μm. The inset shows axonal terminals (Scale: 50 μm). This experiment was repeated in 4 mice. **c** Left: Viral infection (yellow) in CN^{GABA} neurons of *vGat*-Cre mice; bregma: −6.20. Right: CN^{GABA} axonal tracts and terminals in contralateral ZI; bregma: −2.50. Scale: 200 μm. The inset shows the axonal terminals (Scale: 50 μm). This experiment was repeated in 4 mice. **d** Experimental design for retrograde transsynaptic viral injection and immunostaining. **e** The upper panel displays ZI-GLU neurons infected by a virus with a dashed line outlining the ZI area; bregma: −2.50. Scale: 200 μm. Starter cells labeled by EGFP and dsRed are indicated by white arrows. The lower panel shows traced contralateral CN neurons (white arrows) labeled by RV and GABA staining with a dashed line outlining IN and DN; bregma: −6.20. Scale: 25 μm. This experiment was repeated in 4 mice. **f** The proportion of $_{ZI\text{-}GLU}CN$ neurons in the total CN neurons ($n = 30$ sections; 3 mice). **g** The proportions of $_{ZI\text{-}GLU}CN^{GABA}$ and $_{ZI\text{-}Glu}CN^{SMI32}$ neurons ($n = 713$). **h** Upper panel: ZI-GABA neurons infected by virus; bregma: −2.50. Scale: 200 μm. Starter cells were labeled by EGFP and dsRed. Lower panel: traced contralateral CN neurons (bregma: −6.20) labeled by RV virus and SMI32. Note that the enlarged figures have been rotated 90 degrees. Scale: 25 μm. This experiment was repeated in 4 mice. **i** The proportion of $_{ZI\text{-}GABA}CN$ neurons in total CN neurons ($n = 30$ sections; 3 mice). **j** The proportions of $_{ZI\text{-}GABA}CN^{SMI32}$ and $_{ZI\text{-}GABA}CN^{GABA}$ neurons ($n = 951$). Source data are provided as a Source Data file.

responsive tdTomato⁻ neurons (17 out of 48) were completely inhibited by co-application of DNQX and AP5 (Fig. 2c, d). When the command voltage was switched to +40 mV, EPSCs in responding neurons exhibited slow decay kinetics ($\tau = 52.7 \pm 14.5$ ms) and were significantly suppressed by AP5 or fully abolished by AP5 + DNQX (Fig. 2e). These findings indicate that both AMPA and NMDA receptors are postsynaptically present in responsive non-ZI-GLU neurons. Following electrophysiological recordings, single cell RT-PCR (scRT-PCR) was performed to detect mRNA expression in clamped cells. As depicted in Fig. 2f, the *vGluT2* band was exclusively present in tdTomato⁺ cells while the *vGat* band was only detected in responsive tdTomato⁻ cells, confirming that light-stimuli-responsive ZI neurons in the CN^{GLU} → ZI circuit are GABAergic.

We subsequently examined the electrophysiological characteristics of the CN^{GABA} → ZI circuit using *vGat*-Cre;Ai14 mice, which were injected with AAV2/9-FLEX-oChIEF-tdTomato in the CN (Fig. 2a). Patch-clamp recordings were conducted following light stimulation in tdTomato⁺ or tdTomato⁻ ZI neurons. Once again, light stimulation failed to induce current from ZI-GABA (tdTomato⁺) neurons (Fig. 2g), indicating that CN^{GABA} axons do not form connections with ZI-GABA neurons. However, in a subset of non-ZI-GABA (tdTomato⁻) neurons (9 out of 55), light pulses elicited inhibitory postsynaptic currents (IPSCs) that were abolished by TTX (Fig. 2h). Likewise, the non-responsive non-ZI-GABA neurons may lack innervation with CN axons. IPSCs in responsive tdTomato⁻ neurons were restored by the addition of 4AP but blocked by GABAzine (Fig. 2h), a specific antagonist for $GABA_A$ receptors, indicating the monosynaptic connections between CN^{GABA} and non-ZI-GABA neurons and that postsynaptic receptors in non-ZI-GABA neurons consist of $GABA_AR$ subtype. Subsequent scRT-PCR analysis was performed after each recording session, revealing the presence of *vGat* band in tdTomato⁺ cells and *vGluT2* band exclusively in responsive tdTomato⁻ cells (Fig. 2i), suggesting that light-responsive ZI neurons within CN^{GABA} → ZI circuit are glutamatergic.

So far, our results suggest that the CN → ZI circuit consists of two types of synaptic connections: CN^{GLU} neurons project to GABAergic ZI neurons ($_{ZI\text{-}GABA}CN^{GLU}$), while CN^{GABA} neurons project to glutamatergic ZI neurons ($_{ZI\text{-}GLU}CN^{GABA}$) (Fig. 2i).

https://doi.org/10.1038/s41467-025-58727-0

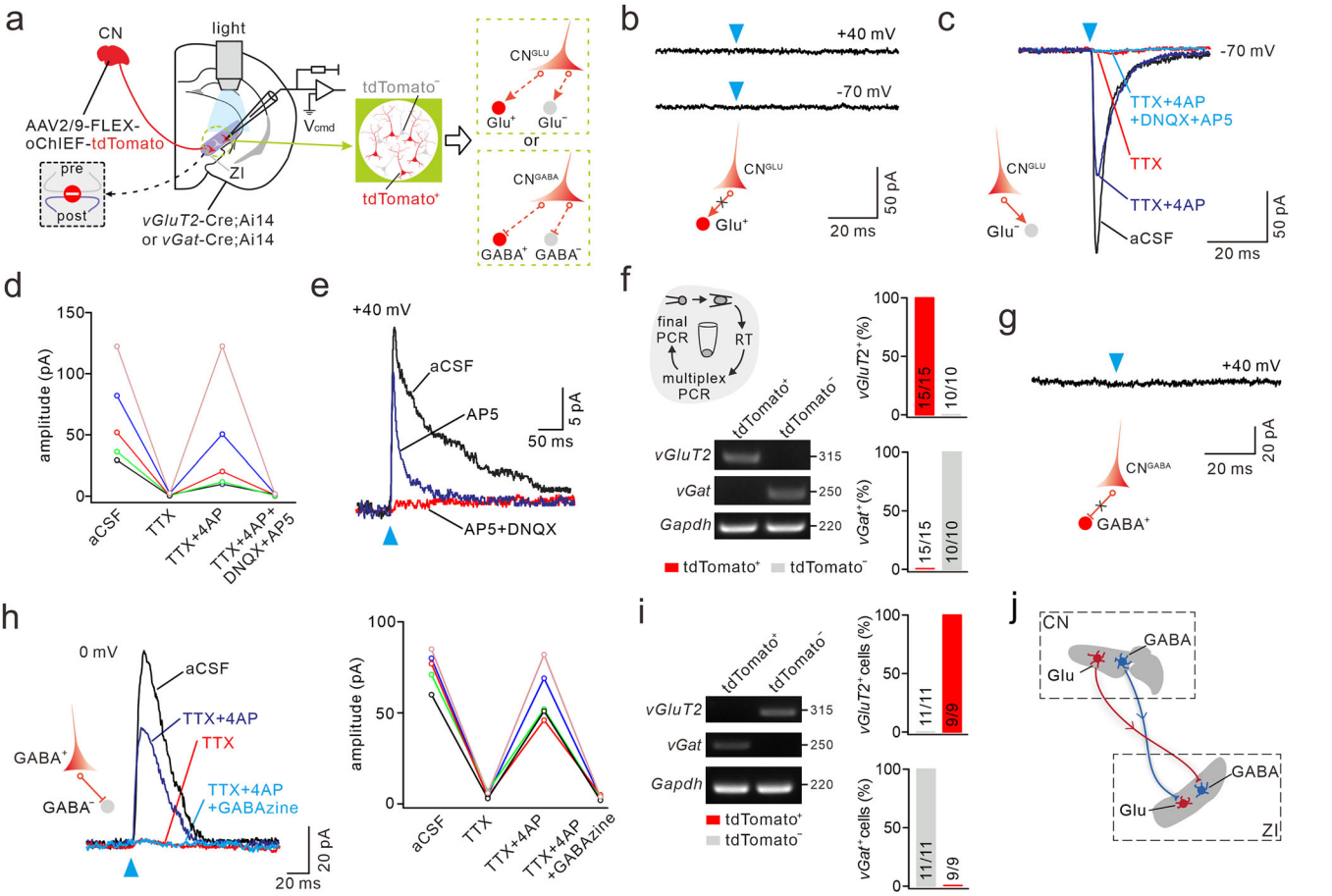

Fig. 2 | CN axons in ZI form monosynaptic glutamatergic and GABAergic synapses. a Schematic of slice recordings in *vGluT2*-Cre;Ai14 or *vGat*-Cre;Ai14 mice. Blue light was delivered to stimulate CN axons in ZI, and recordings were made in either tdTomato$^+$ (Glu$^+$ or GABA$^+$) or tdTomato$^-$ (Glu$^-$ or GABA$^-$) ZI neurons. **b** No response was elicited by light pulse from ZI^{Glu+} neurons clamped at −70 or +40 mV in *vGluT2*-Cre;Ai14 mice ($n = 15$). **c** Monosynaptic responses of ZI^{Glu-} neurons to stimulation of CN axons. Optically evoked responses were blocked by TTX, recovered by 4AP, but eliminated by DNQX + D-AP5. **d** Colors annotate different recorded cells. Averages of peak amplitude: aCSF (64.4 ± 17.1 pA), TTX (1.3 ± 0.3 pA), 4AP + TTX (43.0 ± 21.1 pA), and TTX + 4AP + DNQX + AP5 (1.0 ± 0.3 pA). $n = 5$ neurons per group. **e** Example responses with holding potential at +40 mV. Current amplitude: aCSF (22.1 ± 7.3 pA), AP5 (16.7 ± 4.3 pA), and AP5 + DNQX (1.1 ± 0.4 pA). $n = 5$ neurons per group. **f** scRT-PCR detection of *vGluT2* and *vGat* mRNA expression in patched ZI neurons. Bottom left: representative mRNA bands. Right: percentages of *vGluT2*$^+$ and *vGat*$^+$ ZI^{GABA} in tdTomato$^+$ or tdTomato$^-$ neurons. **g** No response was elicited by light pulse from ZI^{GABA+} neurons clamped at +40 mV in *vGat*-Cre;Ai14 mice ($n = 10$ neurons). **h** Monosynaptic responses of ZI^{GABA-} neurons to stimulation. Colors annotate different recorded cells. Averages of peak amplitude: aCSF (74.6 ± 4.3 pA), TTX (5.0 ± 0.7 pA), 4AP + TTX (60.0 ± 6.7 pA), and TTX + 4AP + GABAzine (3.7 ± 0.5 pA). $n = 5$ neurons per group. **i** scRT-PCR detection in patched ZI neurons. Bottom left: representative mRNA bands. Right: percentages of ZI^{Glu} and ZI^{GABA} in tdTomato$^+$ or tdTomato$^-$ neurons. **j** Schematic showing dual innervations between the CN and ZI. Source data are provided as a Source Data file.

$_{ZI\text{-}GABA}CN^{GLU}$ and $_{ZI\text{-}GLU}CN^{GABA}$ neurons encode stress. It has been reported that DN neurons projecting to the VTA are activated by external stress[26]. Additionally, a recent study demonstrated that the DN neurons projecting to centrolateral amygdala are associated with anxiety[19], which can be induced by stressful situation[1]. These studies have prompted us to investigate whether $_{ZI\text{-}GABA}CN^{GLU}$ and $_{ZI\text{-}GLU}CN^{GABA}$ neurons were activated by stress. To do so, we applied six different stress stimulations (neonatal mouse-induced stress, air puff, overhead object, tail pinch, tail restraint stress, and social attack) to mice (Supplementary Fig. 5a) while simultaneously utilizing fiber photometry to record instant calcium transients of $_{ZI\text{-}GABA}CN^{GLU}$ and $_{ZI\text{-}GLU}CN^{GABA}$ neurons (Supplementary Fig. 5b).

We initially injected AAV2/9Retro-FLEX-Flp into the unilateral ZI of *vGluT2*-Cre mice and AAV-fDIO-GCamp6m into the contralateral CN (Fig. 3a). As a result, $_{ZI\text{-}GABA}CN^{GLU}$ neurons expressed GCamp6m, which produced a green fluorescent signal by binding to intracellular calcium during neuronal activity. An optical fiber was positioned above the CN to record GCamp6m signal (Fig. 3b). Our findings indicated that in response to acute stressors, the activity of $_{ZI\text{-}GABA}CN^{GLU}$ neurons (Ca^{2+} $\Delta F/F$) began to increase upon exposure to stress, reached its peak midway through the stressful event, and remained elevated for some time after the cessation of stimulation (Fig. 3c, d, and f–h). A slightly different pattern of Ca^{2+} dynamics was observed during an overhead object test, with a rapid decline in signal intensity in the middle of the test (Fig. 3e). By summarizing peak $\Delta F/F$ (Fig. 3i), our results indicated that $_{ZI\text{-}GABA}CN^{GLU}$ neurons are capable of encoding stress.

We then injected AAV2/9Retro-FLEX-Flp into the unilateral ZI of *vGat*-Cre mice and AAV-fDIO-GCamp6m into the contralateral CN (Fig. 3j), resulting in the expression of GCamp6m in $_{ZI\text{-}GLU}CN^{GABA}$ neurons. An optical fiber was positioned above the CN to detect GCamp6m signal in mice undergoing various stress tests (Fig. 3k). Notably, stress increased the activity of $_{ZI\text{-}GLU}CN^{GABA}$ neurons to a lesser extent than that observed in $_{ZI\text{-}GABA}CN^{GLU}$ neurons (Fig. 3l–q). These differences were evident not only by a smaller increase in peak $\Delta F/F$, which was approximately 2–3 times less compared to $_{ZI\text{-}GABA}CN^{GLU}$ (Fig. 3r), but also by a shortened duration of Ca^{2+} activation (Fig. 3l–q). These findings demonstrate that both $_{ZI\text{-}GABA}CN^{GLU}$ and $_{ZI\text{-}GLU}CN^{GABA}$ neurons, serving as initiator neurons of glutamatergic and GABAergic

https://doi.org/10.1038/s41467-025-58727-0

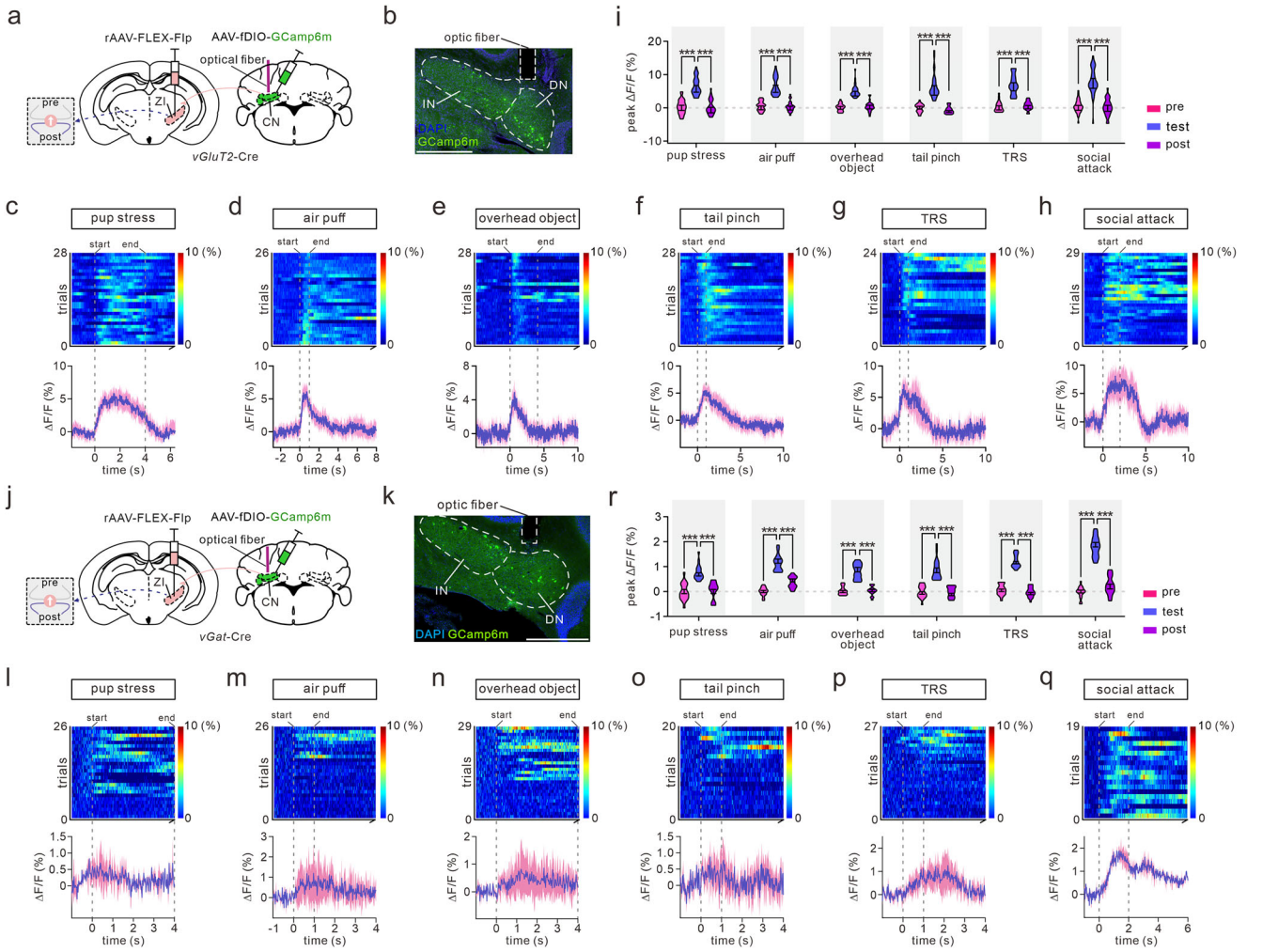

Fig. 3 | $_{ZI\text{-}GABA}CN^{GLU}$ and $_{ZI\text{-}GLU}CN^{GABA}$ neurons are activated by acute stress. **a** Schematic illustrating viral injections in *vGluT2*-Cre mice. **b** Representative image of viral infection and optic fiber implantation in the CN of *vGluT2*-Cre mice. Scale: 200 μM. **c**–**h** in vivo recording of Ca^{2+} activity in $_{ZI\text{-}GABA}CN^{GLU}$ neurons under 6 different stress conditions. Heat maps display Ca^{2+} events in response to stress stimulation. Lower panels present Ca^{2+} transients summarized from all trials, with blue lines indicating the mean and a pink background representing 95% confidence. **i** Peak of Ca^{2+} transients in six stress situations. See Supplementary Table 1 for statistics. $n = 5$ per group. $^{***}p < 0.001$. Two-way ANOVA test. Data: Mean ± SEM. **j** Schematic showing viral injections in *vGat*-Cre mice. **k** Example image displaying viral infection and optic fiber implantation in CN of *vGat*-Cre mice. Scale: 200 μM. **l**–**q** In vivo recording of Ca^{2+} activity in $_{ZI\text{-}GLU}CN^{GABA}$ neurons during 6 stress tests. Heat maps show Ca^{2+} events in response to stress stimuli. Lower panels show summarized Ca^{2+} transients from all trials. **r** Ca^{2+} peak transients in stress situations. See Supplementary Table 2 for statistics. $n = 5$ per group. $^{***}p < 0.001$. Two-way ANOVA test. Data: Mean ± SEM. Source data are provided as a Source Data file.

CN → ZI circuits, respectively, can encode stress stimuli to varying degrees.

To investigate whether $_{ZI\text{-}GABA}CN^{GLU}$ and $_{ZI\text{-}GLU}CN^{GABA}$ neurons respond to emotionally salient stimulation, we employed fiber photometry to record calcium transients in these neurons when the mice were subject to food reward (sucrose pellets) (Supplementary Fig. 6a, b). Our recordings from a 5s-feeding assay revealed no significant changes in GCaMP signals in either $_{ZI\text{-}GABA}CN^{GLU}$ (25 trials; 5 mice) or $_{ZI\text{-}GLU}CN^{GABA}$ (25 trials; 5 mice) neurons before, during, and immediately after the pellet eating (Supplementary Fig. 6c–e). These findings suggest that $_{ZI\text{-}GABA}CN^{GLU}$ and $_{ZI\text{-}GLU}CN^{GABA}$ neurons do not respond to reward consumption.

Activating CN^{GLU} → ZI pathway induces anxiety and aversion. Having demonstrated the activation of $_{ZI\text{-}GABA}CN^{GLU}$ and $_{ZI\text{-}GLU}CN^{GABA}$ neurons in response to stress, we proceeded to investigate the role of CN^{GLU} → ZI pathway on anxiety-like behaviors. To address this question, we expressed oChIEF in bilateral CN and implanted optical fibers targeting bilateral ZI in *vGluT2*-Cre mice, thereby selectively stimulating CN^{GLU} axonal terminals in the ZI (Fig. 4a). The viral expressions in CN neurons and their axonal tracts in the ZI were depicted in Fig. 4b. To determine the role of CN^{GLU} → ZI pathway on anxiety, *vGluT2*-Cre mice expressing only tdTomato (control) or oChIEF were examined in an elevated-plus maze (EPM) (Fig. 4c). Upon light stimulation, oChIEF-expressing mice exhibited significantly reduced open arm entries compared to control mice (Fig. 4c, d). The time spent in the open arm was also decreased in oChIEF-expressing mice following light stimulation (Fig. 4d). In addition, no difference was found in total travel distance between oChIEF-expressing and control *vGlut2*-Cre mice (Fig. 4d). The effects of oChIEF activation were re-evaluated using open field test (OFT) (Supplementary Fig. 7a) and rearing and rotation test (RRT) (Supplementary Fig. 7b). We observed that the photoactivation of CN^{GLU} → ZI circuit reduced mouse exploration in center zone but had no impact on motor speed, travel distance, immobility (Supplementary Fig. 7c), as well as rotation and rearing (Supplementary Fig. 7d).

To validate the findings obtained from optogenetic stimulation, we employed chemogenetic activation of the CN^{GLU} → ZI circuit and assessed anxiety levels of *vGluT2*-Cre mice. Specifically, AAV2Retro-FLEX-Flp was bilaterally injected into the ZI, followed by injection of AAV2/9-hEF1a-fDIO-hM3Dq-mCherry or AAV2/9-hEF1a-fDIO-mCherry

https://doi.org/10.1038/s41467-025-58727-0

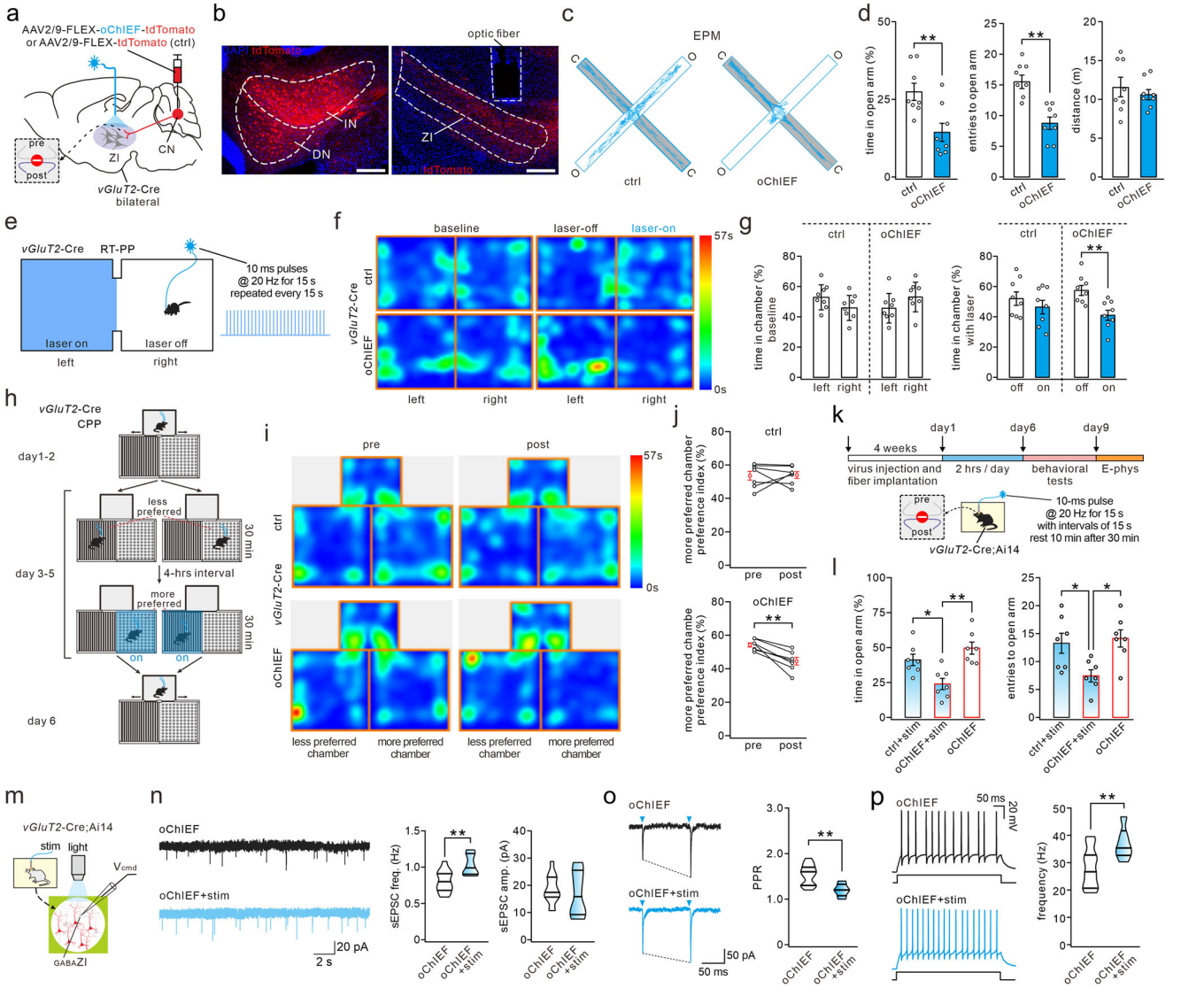

Fig. 4 | Photoactivation of CN^{GLU} → ZI circuit induces anxiety and aversion. **a** Schematic of viral injection in CN and optoactivation of bilateral CN^{GLU} → ZI circuits in *vGluT2*-Cre mice. **b** Example of viral expression in the CN and axon tracts in the ZI. Scale: 200 μm. **c** Activity traces of control and oChIEF-expressing *vGluT2*-Cre mice in EPM with photostimulation (C, close; O, open). **d** Time spent in open arm, entries to open arm, and distance in EPM. $n = 8$ mice per group. One-sided unpaired *t*-test. $^{**}p < 0.01$. Data: mean ± SEM. **e** RTPP and optogenetic stimulation protocol. **f** Representative locomotion traces of control and oChIEF-expressing *vGluT2*-Cre mice in the baseline and the condition of laser-on/off. **g** Percentages of time spent in baseline and photostimulation conditions. $n = 8$ mice per group. One-sided unpaired *t*-test. $^{**}p < 0.01$. Data: mean ± SEM. **h** CPP paradigm for *vGluT2*-Cre mice. **i** Locomotor activity of control and tdTomato-expressing mice before and after CPP training. **j** Percentages of time spent in the more preferred chamber. $n = 7$ mice per group. Two-sided paired *t*-test. $^{**}p < 0.01$. Data: mean ± SEM. **k** Experimental design for inducing artificial anxiety in *vGluT2*-Cre;Ai14 mice. **l** Entries to open arm and time spent in open arm (%) in EPM. $n = 7$ mice per group. One-way ANOVA test. $^{*}p < 0.05$. Data: mean ± SEM. **m** Schematic of whole-cell recording in $_{GABA}$ZI neurons of *vGluT2*-Cre;Ai14 mice with photo stimulation. **n** Representative sEPSC traces recorded from oChIEF-expressing $_{GABA}$ZI neurons in *vGluT2*-Cre;Ai14 mice. oChIEF, $n = 15$. oChIEF + stim, $n = 6$. One-sided unpaired *t*-test. $^{*}p < 0.05$. Data: mean ± SEM. **o** PPR of light-stimulated EPSCs in $_{GABA}$ZI neurons. oChIEF, $n = 15$. oChIEF+stim, $n = 6$. One-sided unpaired *t*-test. $^{**}p < 0.01$. Data: mean ± SEM. **p** Representative population spikes evoked by current injection in oChIEF-expressing $_{GABA}$ZI neurons. oChIEF, $n = 15$. oChIEF+stim, $n = 6$. One-sided unpaired *t*-test. $^{**}p < 0.01$. Data: mean ± SEM. See Supplementary Table 3 for all statistics for this figure. Source data are provided as a Source Data file.

into bilateral CN after a 2-week interval (Supplementary Fig. 8a, b). This resulted in selective modulation of ZI-projecting CN neurons. Subsequently, control and hM3Dq-expressing mice were administered intraperitoneal (i.p.) injection of clozapine-N-oxide (CNO; 2 mg/kg) and subjected to EPM and OFT tests (Supplementary Fig. 8a). Our observations revealed that: (1) chemogenetic activation of the CN^{GLU} → ZI circuit led to reduced entries into and time spent in the open arm for hM3Dq-expressing mice during EPM testing (Supplementary Fig. 8c), with no impact on travel distance; (2) during OFT assessment, chemoactivation of the CN^{GLU} → ZI circuit did not influence motor speed, travel distance, immobility, rotation, or rearing behavior (Supplementary Fig. 8d,e), but notably attenuated exploration within the center zone (Supplementary Fig. 8d). These results corroborate our optogenetic data and support the conclusion that the activation of the CN^{GLU} → ZI circuit induces anxiety without affecting motor function.

Previous studies have demonstrated a positive correlation between aversion and anxiety[27]. Therefore, we investigated whether the CN^{GLU} → ZI pathway induces aversion by conducting place preference tests. We employed two paradigms, real-time place preference (RTPP) to assess short-term stimulation aversion, and conditioned place preference (CPP) to demonstrate conditioned aversion in

vGluT2-Cre mice. In the RTPP experiment, control and oChIEF-expressing *vGluT2*-Cre mice were allowed to freely explore a two-compartment apparatus (Fig. 4e). During baseline without light stimulation, both oChIEF-expressing and control mice exhibited similar preference for each compartment (Fig. 4f, g). Next, one compartment was randomly assigned as the "stimulation compartment": whenever the test mouse entered this compartment, a series of light pulses was automatically administered to activate CN axons in the ZI (Fig. 4e). oChIEF-expressing mice exhibited significantly reduced preference for the stimulation compartment, spending less than 40% of time there (Fig. 4f, g). In contrast, control mice displayed normal preference to both compartments (Fig. 4f, g). During the CPP test, *vGluT2*-Cre mice were given the opportunity to freely explore a divided apparatus with distinct visual cues, thereby developing a relative preference for one of two chambers. Subsequently, the mice underwent conditioning over three consecutive days: they were confined to the less-preferred chamber for 30 min without any stimulation and to the more preferred chamber for 30 min while fiber optics delivered light stimuli to activate ZI-projecting CN axons (Fig. 4h). Following conditioning, oChIEF-expressing mice spent substantially less time in the more preferred compartment (Fig. 4i, j), whereas control mice were unaffected by conditioning and maintained their bias for each side (Fig. 4i,j).

If $CN^{GLU} \rightarrow ZI$ circuit is found to regulate anxiety in behaving mice, we could potentially manipulate their emotional state by artificially activating this circuit in the absence of real anxiety experience. To test this hypothesis, optic fibers were implanted over bilateral ZI in control and oChIEF-expressing *vGluT2*-Cre;Ai14 mice, followed by a 20-Hz photostimulation (2 h/day) at the $CN \rightarrow ZI$ terminals for consecutive 5 days in freely moving mice, and their behaviors and electrophysiological properties were assessed later (Fig. 4k). Interestingly, pure photostimulation drastically reduced the duration and entries to open arm in oChIEF-expressing mice. In contrast, the behavioral phenotypes of either control mice with stimulation or oChIEF-expressing mice without stimulation remained unchanged (Fig. 4l). These data strongly suggest that solely activating the CN^{GLU}-ZI circuit can induce an artificial "anxiety experience", resulting in "anxious mice". Further behavioral tests showed that such artificial stimulation did not affect motor activities, because: (1) total travel distance in EPM was unaffected (Supplementary Fig. 9a); (2) all parameters in OFT, such as motor speed, travel distance, immobility, and center zone time were similar to those of the control group (Supplementary Fig. 9b); (3) light stimulation during the rotarod test did not impact time on the rod with increasing revolutions (Supplementary Fig. 9c); and (4) no abnormal rearing or rotation was observed among groups of mice tested (Supplementary Fig. 9d). It should be noted that unlike EPM results, there was no statistical difference in center zone time among three groups of mice during OFT test (Supplementary Fig. 9b). This may be because EPM is more sensitive than OFT when detecting levels of anxiety[28].

To investigate the electrophysiological characteristics of the $CN^{GLU} \rightarrow ZI$ pathway in *vGluT2*-Cre;Ai14 mice subjected to pure photostimulation, patch-clamp recordings were conducted in $_{ZI\text{-}GABA}CN^{GLU}$ neurons (Fig. 4m), which were responsive to light stimulation (Fig. 2c). Our findings revealed that artificial photostimulation increased the frequency of spontaneous EPSCs (sEPSCs) in $_{ZI\text{-}GABA}CN^{GLU}$ neurons from oChIEF-expressing mice, while the amplitude of sEPSCs remained unchanged (Fig. 4n). These results suggest an enhanced presynaptic release caused by conditioned $CN^{GLU} \rightarrow ZI$ axonal stimuli, as supported by a reduction in paired-pulse ratio (PPR) of evoked EPSCs following in vivo photostimulation in oChIEF-expressing mice compared to controls (Fig. 4o), suggesting a presynaptic form of long-lasting potentiation at CN^{GLU}-ZI synapses (LTP^{Pre}_{GLU}). LTP^{Pre}_{GLU} was observed not only on day one but also on day four after the artificial anxiety experience (Fig. 4n–p and Supplementary Fig. 10–g). Furthermore, our investigation into the impact of photostimulation on postsynaptic ZI neurons revealed a significant decrease in interspike interval (ISI), indicative of enhanced excitability[29], upon artificial photostimulation in oChIEF-expressing mice (Fig. 4p). In summary, these data demonstrate that conditioned in vivo stimulations activate the $CN^{GLU} \rightarrow ZI$ circuit, leading to LTP^{Pre}_{GLU} and increased intrinsic excitability of postsynaptic ZI neurons, providing insight into the cellular basis for anxiety and aversion.

Silencing $CN^{GLU} \rightarrow ZI$ pathway reduces anxiety. The effects of activating the $CN^{GLU} \rightarrow ZI$ circuit prompted us to investigate whether silencing this circuit can suppress anxiety. To do so, we bilaterally injected non-transsynaptic AAV2/9-DIO-NpHR-EYFP or AAV2/9-DIO-EYFP (control) into the CN and applied yellow light stimulation to CN^{GLU} terminals in bilateral ZI of *vGluT2*-Cre mice (Fig. 5a). With this setup, glutamatergic CN neurons and their axonal terminals expressed NpHR, allowing selective inhibition by optic fibers over the ZI (Fig. 5b). Anxiety levels of control and NpHR-expressing mice were tested using EPM (Fig. 5c). Compared to control mice, NpHR-expressing mice exhibited more entries to and spent more time in the open arm upon light stimulation (Fig. 5c, d). Total travel distance did not differ between the two groups (Fig. 5d). These mice were also tested in OFT and RRT, where motor speed, travel distance, immobility, center zone time in OFT, rearing and rotation were all unchanged in NpHR-expressing mice compared to control mice (Fig. 5e, f). The modulatory effects of the $CN^{GLU} \rightarrow ZI$ circuit were also investigated in the mice with anxiety. In *vGluT2*-Cre mice, AAV2/9-DIO-NpHR-EYFP or AAV2/9-DIO-EYFP was injected into the CN and optic fibers were implanted in bilateral ZI, and anxiety-like behavior was induced through acute restraint stress (ARS) for 2 h (Supplementary Fig. 11a, b), as described previously[30]. NpHR-expressing ARS mice exhibited more center zone time in the OFT than EYFP-expressing ARS mice, whereas motor speed, travel distance, and immobility were unchanged (Supplementary Fig. 11c). Likewise, NpHR-expressing ARS mice had more entries to and spent more time in the open arm than EYFP-expressing ARS mice (Supplementary Fig. 11d). These results indicate that the $CN^{GLU} \rightarrow ZI$ circuit exerts effects in the mice with anxiety.

Next, we utilized the chemogenetics method to inhibit the $CN^{GLU} \rightarrow ZI$ circuit in *vGluT2*-Cre mice and assessed their anxiety levels and motor activity. AAV2/9-hEF1a-fDIO-hM4Di-mCherry or AAV2/9-hEF1a-fDIO-mCherry (control) was injected into bilateral CN two weeks after the injection of AAV2Retro-FLEX-Flp in bilateral ZI (Supplementary Fig. 12a, b). Following i.p. injection of CNO, both control and hM4Di-expressing mice underwent EPM, OFT and RRT studies (Supplementary Fig. 12a). In the EPM test, chemoinhibition of the $CN^{GLU} \rightarrow ZI$ projection resulted in increased entries to and time spent in the open arm for hM4Di-expressing mice, while their travel distance remained unchanged (Supplementary Fig. 12c). In the OFT, chemoinhibition did not impact motor speed, travel distance, immobility, or exploration in the center zone for hM4Di-expressing mice (Supplementary Fig. 12d). Finally, rearing and rotation were also unaltered in RRT testing (Supplementary Fig. 12e). These results align with optoinhibition experiments suggest that silencing the $CN^{GLU} \rightarrow ZI$ circuit has potential to alleviate anxiety.

We next injected Cre-dependent tetanus toxin light chain (TetTox) into the CN of *vGluT2*-Cre mice to specifically block vesicle-mediated synaptic release of ZI-projecting glutamatergic CN neurons. AAV2Retro-FLEX-Flp was injected into bilateral ZI, followed by injection of AAV2/9-fDIO-TetTox-mCherry or AAV2/9-fDIO-mCherry (control) into bilateral IN/DN two weeks later (Supplementary Fig. 13a, b). In the EPM test, we observed that blocking $CN^{GLU} \rightarrow ZI$ synaptic transmission significantly increased the entries to and time spent in open arm of TetTox-expressing mice, while mouse travel distance remained unchanged (Supplementary Fig. 13c). No significant effects were observed on motor speed, travel distance, immobility, or time in the center zone in TetTox-expressing mice in OFT (Supplementary Fig. 13d), and rearing and rotation were also unaltered (Supplementary

https://doi.org/10.1038/s41467-025-58727-0

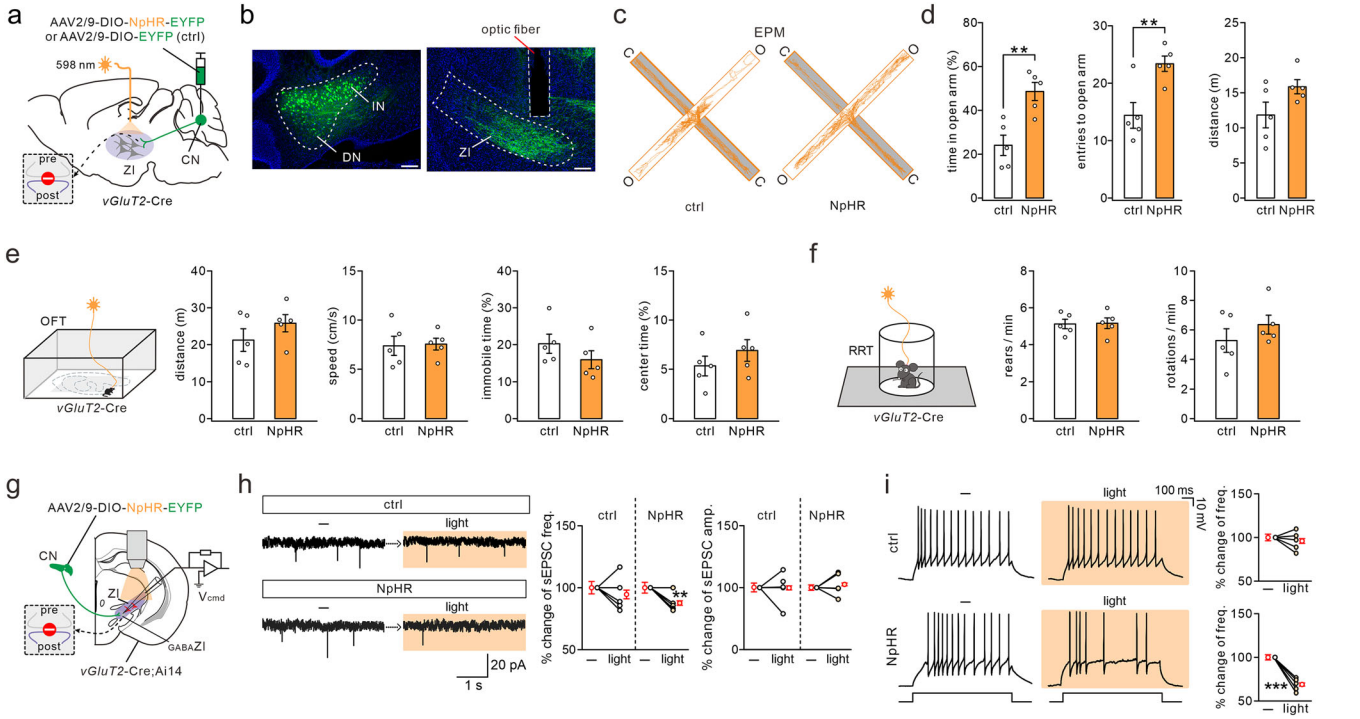

Fig. 5 | Photoinhibition of CN^{GLU} → ZI circuit reduces anxiety. a Schematic of viral injection in CN and optogenetic inhibition of bilateral CN^{GLU} → ZI circuits. **b** Examples of viral expression in the CN and axonal tracts in the ZI. Scale: 200 μm. **c** Activity traces of *vGluT2*-Cre mice in EPM with photoinhibition. **d** Time spent in open arm, entries to open arm, and distance in EPM. $n = 5$ mice per group. One-sided unpaired *t*-test. $^{**}p < 0.01$. Data: mean ± SEM. **e** *vGluT2*-Cre mice received optoinhibition during OFT. $n = 6$ mice per group. One-sided unpaired *t*-test. Data: mean ± SEM. **f** *vGluT2*-Cre mice received optoinhibition during RRT. $n = 6$ mice per group. One-sided unpaired *t*-test. Data: mean ± SEM. **g** Schematic of recording in tdTomato$^-$ ZI neurons. **h** Representative sEPSCs with (light)/without (−) light inhibition (recording interval: 1 min). $n = 5$ cells from three mice per group. Two-sided paired *t*-test. $^{**}p < 0.01$. Data: mean ± SEM. **i** Representative population spikes in control or NpHR-expressing neurons with (light)/without (−) light inhibition. $n = 5$ cells from three mice per group. Two-sided paired *t*-test. $^{***}p < 0.001$. Data: mean ± SEM. See Supplementary Table 4 for all statistics for this figure. Source data are provided as a Source Data file.

Fig. 13e). These results further support the role of CN^{GLU} → ZI synaptic transmission in anxiety regulation.

To investigate the cellular mechanism of CN^{GLU} → ZI pathway inhibition on mouse performance, we conducted ex vivo recording to assess synaptic efficacy (Fig. 5g). Using voltage- and current-clamp configurations, we examined $_{GABA}$ZI^{CN} neurons in *vGluT2*-Cre;Ai14 mice (5 out of 17 clamped cells) (Fig. 5g), which were confirmed by *post hoc* scRNA test (data not shown). Our findings revealed that photoinhibiton led to a reduction in sEPSC frequency in $_{GABA}$ZI^{CN} neurons from NpHR-expressing mice, while sEPSC amplitude remained unchanged across all $_{GABA}$ZI neurons obtained from control mice (Fig. 5h). Furthermore, our analysis of intrinsic excitability showed a significant decrease in firing rates among those $_{GABA}$ZI neurons that exhibited reduced sEPSC upon light stimulation ($_{GABA}$ZI^{CN}; 5 out of 5) in NpHR-expressing mice (Fig. 5i). Overall, these results indicate that the photoinhibition of the CN^{GLU}-ZI circuit can attenuate both synaptic transmission and intrinsic excitability of $_{GABA}$ZI^{CN} neurons.

Activation of CN^{GABA} → ZI circuit attenuates anxiety and aversion. Subsequently, we sought to investigate the potential involvement of the CN^{GABA} → ZI circuit in anxiety. To address this question, AAV2/9-FLEX-oChIEF-tdTomato or AAV2/9-FLEX-tdTomato (control) was bilaterally injected into the CN, and optical fibers were implanted over bilateral ZI in *vGat*-Cre mice (Fig. 6a). Consequently, oChIEF expression was observed in GABAergic CN neurons, as well as their axonal terminals in the ZI (Fig. 6b), thereby facilitating the activation of CN^{GABA} → ZI terminals through optical fibers. Subsequent testing of mice with viral injection was conducted using EPM with optogenetic stimulation (Fig. 6c). The optogenetic stimulation resulted in a reduction of anxiety in oChIEF-expressing mice, which displayed increased entries to and time spent in the open arm compared to control mice (Fig. 6c, d). There was no difference observed between groups regarding travel distance (Fig. 6d). These findings indicate that activating CN^{GABA} → ZI circuit has anxiolytic effects. The roles of CN^{GABA} → ZI circuit were also examined in OFT (Supplementary Fig. 14a) and RRT (Supplementary Fig. 14b). Photoactivation of CN^{GABA} → ZI circuit did not change mouse exploration in the center zone (Supplementary Fig. 14c), suggesting that it may have a weaker impact on anxiety levels. Additionally, no changes were observed regarding motor speed, travel distance, immobility (Supplementary Fig. 14c), and rotation and rearing behavior among oChIEF-expressing mice (Supplementary Fig. 14d).

Modulatory effects of the CN^{GABA} → ZI circuit were further investigated in the mice with anxiety. In *vGat*-Cre mice, AAV2/9-FLEX-oChIEF-tdTomato or AAV2/9-FLEX-tdTomato was injected into the CN and optic fibers were implanted in bilateral ZI, and anxiety behavior was induced using ARS for 2 h (Supplementary Fig. 11a, b). oChIEF-expressing ARS mice exhibited more center zone time in the OFT than tdTomato-expressing ARS mice, whereas motor speed, travel distance, and immobility were unchanged (Supplementary Fig. 11f). oChIEF-expressing ARS mice had more entries to and spent more time in the open arm than tdTomato-expressing ARS mice (Supplementary Fig. 11g). These results indicate that the CN^{GABA} → ZI circuit exerts effects in the mice with anxiety.

Next, we asked whether the CN^{GABA} → ZI circuit is involved in place preference using RTPP and CPP paradigms. In the RTPP test, oChIEF-expressing mice exhibited a "rewarding" preference by spending over 60% of their time in the stimulation compartment, while control mice showed no bias towards the stimulation chamber (Fig. 6e, f). During the CPP, *vGat*-Cre mice were also allowed to develop a relative

https://doi.org/10.1038/s41467-025-58727-0

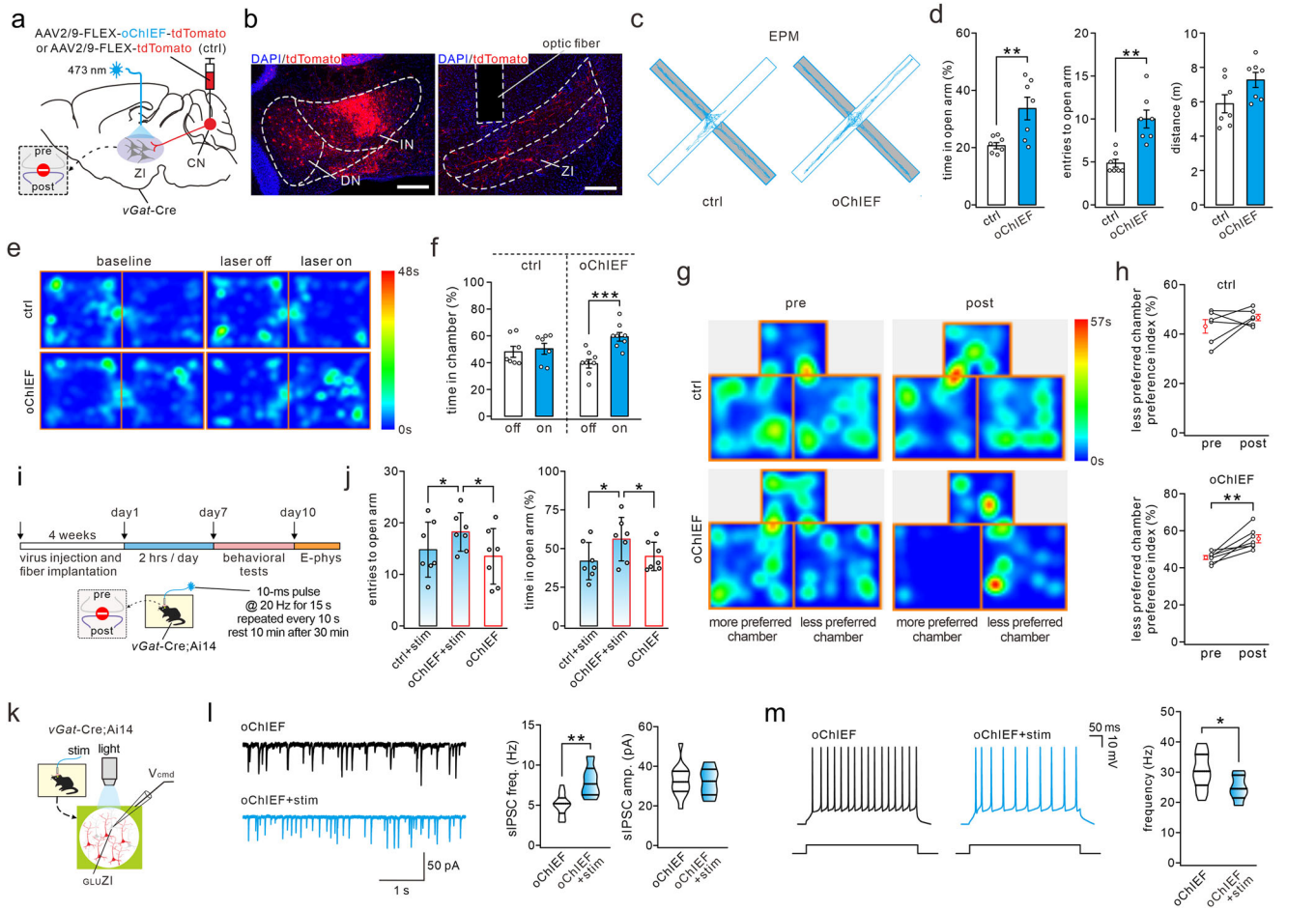

Fig. 6 | Photoactivation of CN^{GABA} → ZI circuit reduces anxiety and induces reward. a Schematic of viral injection in the CN and optogenetic stimulation of bilateral CN^{GABA} → ZI pathway in *vGat*-Cre mice. **b** Examples of viral expression in the CN and axonal tracts in the ZI. An optic fiber was positioned above ZI to stimulate CN^{GABA} axons. Scales: 200 μm. **c** Representative activity traces of control and oChIEF-expressing *vGat*-Cre mice in EPM with photostimulation. **d** Time spent in open arm, entries to open arm, and distance in EPM. $n = 7$ mice per group. One-sided unpaired *t*-test. $^{**}p < 0.01$. $^{***}p < 0.001$. Data: mean ± SEM. **e** Representative locomotor traces of tdTomato- or oChIEF-expressing *vGat*-Cre mice in the baseline (left) and the conditions of laser-on/off (right). **f** Percentages of time spent during photostimulation. Control, $n = 7$ mice per group. oChIEF, $n = 8$ mice per group. One-sided unpaired *t*-test. $^{***}p < 0.001$. Data: mean ± SEM. **g** Locomotor traces of tdTomato- and oChIEF-expressing *vGat*-Cre mice in CPP. **h** Percentages of time spent in the less preferred chamber. Control, $n = 6$ mice per group. oChIEF, $n = 7$ mice per group. Two-sided paired *t*-test. $^{**}p < 0.01$. Data: mean ± SEM. **i** Experimental design for artificially inhibiting anxiety in *vGat*-Cre;Ai14 mice. **j** Entries to open arm and time spent in open arm (%) in EPM. $n = 7$ mice per group. One-way ANOVA test. $^{*}p < 0.05$. Data: mean ± SEM. **k** Schematic of whole-cell recording in $_{GLU}$ZI neurons with photo stimulation. **l** Representative sIPSCs recorded from oChIEF-expressing and oChIEF-expressing+stimulation neurons in *vGat*-Cre;Ai14 mice. oChIEF, $n = 15$. oChIEF+stim, $n = 6$. One-sided unpaired *t*-test. $^{**}p < 0.01$. Data: mean ± SEM. **m** Representative population spikes evoked by current injection in tdTomato- and oChIEF-expressing neurons. oChIEF, $n = 15$. oChIEF + stim, $n = 6$. One-sided unpaired *t*-test. $^{*}p < 0.05$. Data: mean ± SEM. See Supplementary Table 5 for all statistics for this figure. Source data are provided as a Source Data file.

preference for one of the two chambers, and underwent conditioning over three consecutive days: they were confined to the more preferred chamber for 30 min without any stimulation and to the less preferred chamber for 30 min while light stimuli were delivered to activate ZI-projecting CN axons (Supplementary Fig. 15). Following conditioning, oChIEF-expressing mice spent significantly more time in the stimulation compartment after conditioning, whereas control mice maintained their bias towards each chamber (Fig. 6g, h). These findings indicate that activation of the CN^{GABA} → ZI circuit results in a rewarding effect rather than aversion.

At this point, we became intrigued by the question of whether artificially activating the CN^{GABA} → ZI circuit could induce emotions without real experience. Thus, optic fibers were bilaterally implanted over the ZI in oChIEF- or tdTomato-expressing *vGat*-Cre; Ai14 mice, and 20-Hz photostimulation (repeated every 10 s; 2 h per day) was administered to CN^{GABA} → ZI terminals in freely moving mice for 7 consecutive days (Fig. 6i), a stimulation intensity greater than that for *vGluT2*-Cre mice. We observed that this artificial stimulation of CN^{GABA} → ZI resulted in an anxiolytic effect in oChIEF-expressing mice, as evidenced by a significant increase in entries to and duration spent in the open arm of EPM (Fig. 6j), contrary to stimulating CN^{GLU} → ZI.

The findings above strongly suggest that the CN^{GABA} → ZI transmission may also undergo an LTP process with anxiolytic effects. To test this assumption, we conducted electrophysiological studies on the CN^{GABA} → ZI pathway in *vGat*-Cre;Ai14 mice that had received artificial photostimulations, using patch recordings in $_{ZI\text{-}GLU}$CN^{GABA} neurons (Fig. 6k), which were confirmed by evoked IPSC in response to light stimulation. We observed a significant increase in sIPSC frequency of $_{ZI\text{-}GLU}$CN^{GABA} neurons from oChIEF-expressing mice compared to control mice following photostimulation (Fig. 6l). This result indicates the presence of a presynaptic form of GABAergic synaptic LTP (LTP$^{Pre}_{GABA}$) in the CN^{GABA} → ZI circuit. LTP$^{Pre}_{GABA}$ was observed not only on day one but also on day four after the artificial anxiety experience (Fig. 6l and Supplementary Fig. 10h–l). Furthermore, we

examined the effect of LTP^{Pre}_{GABA} on $_{GLU}ZI^{CN}$ neurons by assessing their intrinsic excitability. As shown in Fig. 6m, artificial stimulations attenuated the firings of $_{GLU}ZI^{CN}$ neurons in oChIEF-expressing mice compared to control mice. This finding provides compelling evidence that LTP^{Pre}_{GABA} can impact the intrinsic properties of ZI neurons.

CN → ZI circuits mediate motor-induced alleviation of anxiety. Having established the responses of CN neurons to stress, we proceeded to investigate the functionality of CN → ZI circuits under natural stimulation in mice. It has been demonstrated that challenging motor activity can activate DN neurons[19]. This finding prompted us to consider whether CN → ZI projections are also involved in regulating motor-induced anti-anxiety.

First, WT mice underwent rotarod running twice a day for 4 days at an initial speed of 5 rpm and an acceleration of 9 rpm, followed by an anxiety test (Fig. 7a). This paradigm allowed us to investigate the impact of motor activity on anxiety-like behavior. Our results revealed that, during EPM test, motor mice displayed increased entry into and more time spent in the open arm compared to non-motor mice (Fig. 7b). Additionally, there was no difference in walking distance between two groups, ruling out the influence of energy depletion (Fig. 7b). These results are consistent with the previous work showing that challenging motor can mitigate anxiety level[19].

Next, we investigated whether manipulating CN^{GLU} → ZI and CN^{GABA} → ZI pathways can mediate the motor-induced reduction in anxiety. We selected to chemogenetically activate the CN^{GLU} → ZI pathway or inhibit the CN^{GABA} → ZI pathway, as either manipulation is expected to reverse the motor-induced alleviation of anxiety. In *vGluT2*-Cre mice, AAV-fDIO-hM3Dq-mCherry or AAV-fDIO-mCherry was bilaterally injected into the CN two weeks after the injection of rAAV-FLEX-Flp in bilateral ZI (Fig. 7c). Following CNO injection, the mice were divided into three groups: AAV-fDIO-mCherry (control), AAV-fDIO-mCherry plus rotarod running (run), and AAV-fDIO-hM3Dq-mCherry plus rotarod running (run+hM3Dq) (Fig. 7c). Here, CNO-induced excitation occurred before rotarod running. We observed that, similar to WT mice (Fig. 7b), *vGluT2*-Cre mice receiving AAV-fDIO-mCherry also exhibited increased entry into and prolonged time spent in the open arm following motor activity, compared to control mice without running (Fig. 7d). The chemoactivation of CN^{GLU} → ZI pathway significantly mitigated the anxiolytic effect, resulting in entry into and time spent close to control levels. Once again, there was no distinction in EPM distance among the three groups (Fig. 7d). These findings indicate that activating CN^{GLU} → ZI circuit is sufficient to modulate motor-induced alleviation of anxiety.

Next, we chemogenetically inhibited the CN^{GABA} → ZI pathway to investigate its role in motor-induced anxiolytic effect. AAV-fDIO-hM4Di-mCherry or AAV-fDIO-mCherry was bilaterally injected into the CN two weeks after the injection of rAAV-FLEX-Flp in bilateral ZI of *vGat*-Cre mice (Fig. 7e). Similarly, three groups, AAV-fDIO-mCherry, AAV-fDIO-mCherry plus running, and AAV-fDIO-hM4Di-mCherry plus running (run+hM4Di), were created for the mice with CNO injection (Fig. 7e). Note that CNO-induced inhibition occurred before rotarod running. Likewise, motor activity promoted entry into and prolonged time spent in the open arm of *vGat*-Cre mice receiving AAV2/9-fDIO-mCherry (Fig. 7f); chemoinhibition of the CN^{GABA} → ZI pathway reduced the anxiolytic effect caused by motor activity, showing decreased entry into and time spent compared to control plus running group (Fig. 7f). There was no difference in EPM distance among three groups (Fig. 7f). These results indicate that suppressing CN^{GABA} → ZI circuit is also sufficient to modulate motor-induced alleviation of anxiety.

The separate effects of CN^{GLU} → ZI and CN^{GABA} → ZI circuits on exercise-induced anxiety alleviation raise two new questions: (1) Is the CN → ZI circuit activated during exercise? (2) How does the entire CN → ZI pathway modulate exercise-induced anxiety alleviation? To address these questions, we firstly investigated the influence of rotarod running on the projection strength of the CN → ZI pathway. Anterograde and nontranssynaptic AAV2/9-hSyn-oChIEF-tdTomato were injected into the CN of WT mice, and an optrode was lowered to the contralateral ZI three weeks later (Fig. 7g). In vivo local field potentials (LFPs) of the CN → ZI pathway were recorded before and after 4-day rotarod running, upon light stimulation at the CN → ZI circuitry terminals of these mice (Fig. 7g). In both the control group (without running) and the running group, the LFP of the CN → ZI projection could be strongly recorded with a similar amplitude upon light stimulation (Fig. 7h). Interestingly, there was a significant increase in the LFP for mice with running experience, while no change was observed in those mice without running (Fig. 7h, i). These results suggest that the strength of the total CN outputs to the ZI is enhanced by rotarod running.

Secondly, to explore the effect of the entire CN → ZI pathway on motor-induced anxiety alleviation, AAV-hSyn-hM4Di-mCherry or AAV-hSyn-mCherry was bilaterally injected into the CN, and CNO was locally administered into bilateral ZI using a cannula in WT mice. As a result, three groups were established: AAV-hSyn-mCherry, AAV-hSyn-mCherry plus running, and AAV-hSyn-hM4Di-mCherry plus running (run+hM4Di) (Fig. 7j). Once again, motor activity facilitated the entry and prolonged the time spent in the open arm of WT mice receiving AAV-mCherry (Fig. 7k). In contrast, chemoinhibition of the entire CN → ZI pathway significantly elevated the anxiolytic effect induced by motor activity (Fig. 7k). Additionally, there was no disparity in EPM distance among the three groups (Fig. 7k). These findings indicate that inhibiting entire CN → ZI circuit leads to anxiety relief, which might be driven by the override of the CN^{GABA} → ZI^{GLU} circuit by the CN^{GLU} → ZI^{GABA} circuit.

Discussion

The present work uncovers a previously unrecognized role of CN → ZI circuits in regulating anxiety-like behaviors in mice. Our findings demonstrate that: (i) CN neurons send projections to the ZI through both CN^{GLU} → ZI^{GABA} and CN^{GABA} → ZI^{GLU} transmissions; (ii) controlling CN^{GLU} → ZI^{GABA} and CN^{GABA} → ZI^{GLU} circuits can bidirectionally regulate anxiety and place preference; (iii) repeated stimulations induce presynaptic LTP in both glutamatergic and GABAergic CN → ZI circuits, leading to either increased or decreased anxiety levels; and (iv) CN^{GLU} → ZI^{GABA} and CN^{GABA} → ZI^{GLU} circuits are sufficient to modulate motor-induced alleviation of anxiety. Meanwhile, we provide compelling data to indicate that both CN^{GLU} → ZI^{GABA} and CN^{GABA} → ZI^{GLU} circuits are not involved in motor activity. Our results, along with recent work demonstrating the involvement of a hypothalamo-cerebello-amygdalar circuit in motor-induced alleviation of anxiety[19], underscore the close relationship between the cerebellum and anxiety.

Features of CN → ZI projections

The majority of connections between two brain regions are typically characterized by a single type of neurotransmitter, although they may project to more than one type of target neuron. Surprisingly, our results from multiple lines of evidence support the prevalence of both glutamatergic and GABAergic projections in the CN → ZI circuit, with receiving neurons containing opposite neurotransmitters. We hypothesize that this complex structural organization may arise from the presence of abundant neuronal types in both the CN as the originating area and ZI as the target area, and particular mechanisms during the development. However, it remains unclear why these opposing projections are maintained in cerebellar outputs.

It is widely believed that long-range axons to distant brain areas derive by and large from glutamatergic neurons. Nevertheless, an increasing number of reports provide evidence that, apart from well-studied interneurons, a small subset of GABAergic neurons also sends long-range axons to synchronize distant brain areas for efficient information transmission and processing[31]. To date, the vast majority

https://doi.org/10.1038/s41467-025-58727-0

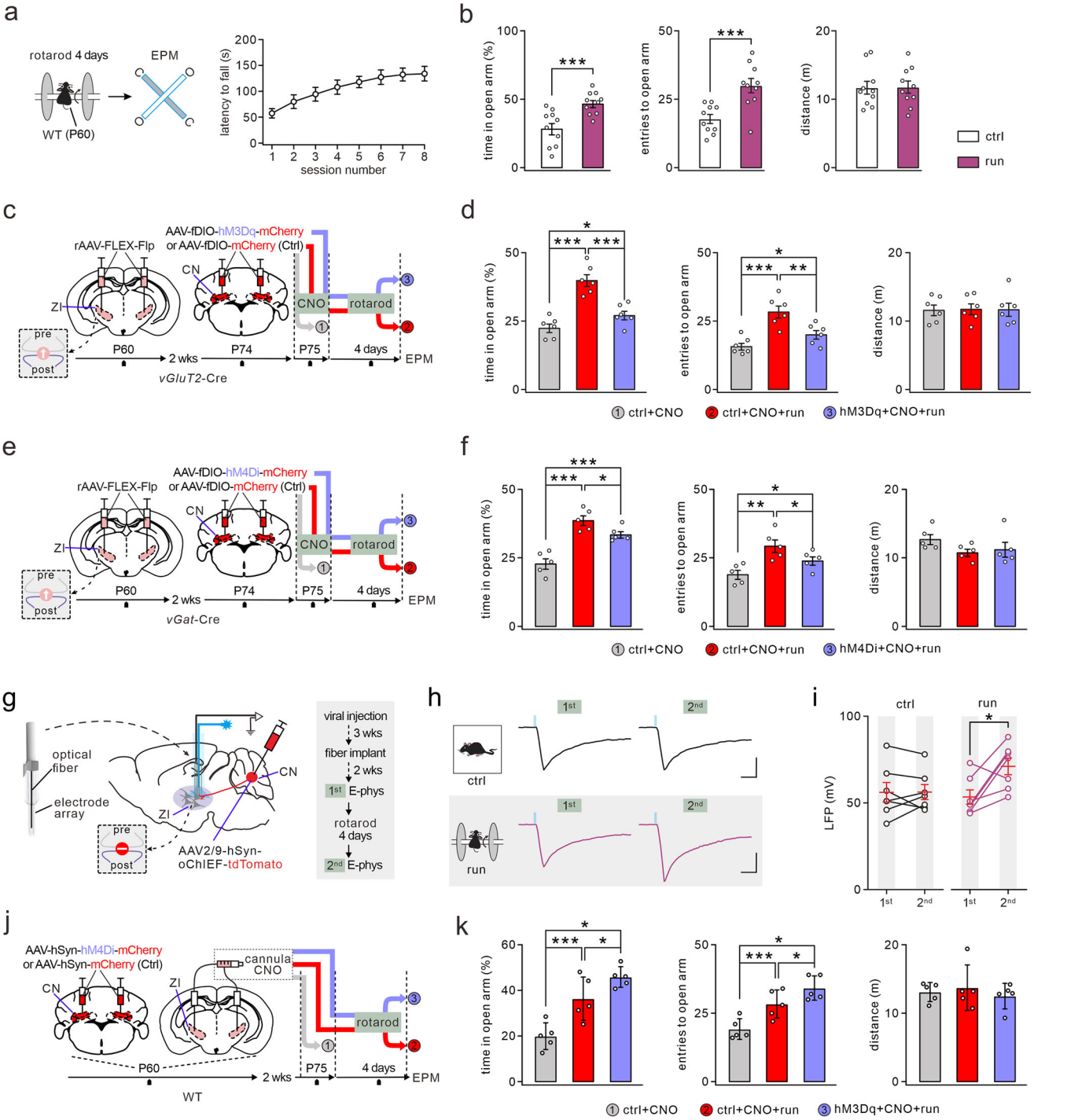

Fig. 7 | CN → ZI circuits regulate rotarod running-induced anxiolytic effect. **a** Rotarod and EPM in WT mice. Latency to fall (s): 57.3 ± 9.5 (#1), 81.5 ± 13.9 (#2), 94.1 ± 14.1 (#3), 107.7 ± 13.9 (#4), 117.2 ± 11.2 (#5), 126.9 ± 15.7 (#6), 131.3 ± 13.1 (#7), 133.3 ± 14.9 (#8). $n = 6$ mice/session. Data: mean ± SEM. **b** Time in open arm (%): 28.9 ± 4.3 (control) and 47.2 ± 2.7 (run), $p = 0.0007$. Entries to open arm: 17.8 ± 1.7 (control) and 30.0 ± 2.8 (run), $p = 0.00047$. Distance: 11.7 ± 1.0 m (control) and 11.8 ± 0.9 m (run), $p = 0.47$. $n = 10$ mice/group. One-sided unpaired t-test. Data: mean ± SEM. **c** Schematic illustrating retrograde and Cre-inducible hM3Dq injection, as well as CNO injection for impact on running-induced anxiolytic effects. CNO-induced excitation was before the rotarod test. **d** Chemogenetic activation of CN^{GLU} → ZI projections inhibited the anxiolytic effect induced by running. $n = 6$ mice/group. One-way ANOVA test. Data: mean ± SEM. **e** Schematic showing retrograde and Cre-inducible hM4Di viral injection, as well as CNO injection, followed by their impact on running-induced anxiolytic effect. CNO-induced inhibition was before rotarod. **f** Chemoinhibition of CN^{GABA} → ZI projections inhibited the anxiolytic effect caused by running. $n = 5$ mice/group. One-way ANOVA test. Data: mean ± SEM. **g** AAV2/9-hSyn-oChIEF-tdTomato was injected into the CN, followed by optrode implantation. Photo-induced LFP of CN → ZI pathway was measured in the same mouse. **h** Representative LFPs induced by light (2 ms) from control and running groups. **i** First and second LFP recordings. Control: 56.1 ± 6.1 mV (1st) and 56.3 ± 4.7 mV (2nd), $p = 0.98$. Running: 53.4 ± 4.4 mV (1st) and 71.1 ± 5.2 mV (2nd), $p = 0.016$. $n = 7$ mice/group. Two-sided paired t-test. Data: mean ± SEM. **j** hM4Di injection and cannula-based CNO injection followed by running-induced anxiolytic effect. **k** Chemoinhibition of CN → ZI projections enhanced anxiolytic effect. $n = 5$ mice/group. One-way ANOVA test. Data: mean ± SEM. $^{*}p < 0.05$. $^{**}p < 0.01$. $^{***}p < 0.001$. See Supplementary Table 6 for all statistics. Source data are provided as a Source Data file.

of long-range GABAergic inhibitory neurons have been identified in cortico-cortical and cortico-subcortical networks such as the hippocampus, amygdala, and medial septum[32]. However, while GABAergic projection has been recognized in the cerebello-vestibular efferent system[33], long-range GABAergic projection similar to that found in cortical networks has scarcely been reported in the cerebellum. Our results clearly indicate long-range GABAergic projections in the CN → ZI pathway with a linear bregma distance between two regions of roughly 4 mm according to the brain map, which significantly promotes our understanding of long-range GABAergic projections. Yet, one intriguing question remains: to what extent CN long-range GABAergic neurons simultaneously regulate both local CN and remote ZI regions, thereby enhancing inter-regional integration in information processing within the cerebello-cerebral network.

Strikingly, we observed that, in naive mice, stimulation of CN axons induces presynaptic form of LTP at both $CN^{GLU} \rightarrow ZI^{GABA}$ and $CN^{GABA} \rightarrow ZI^{GLU}$ synapses, subsequently impacting intrinsic excitability of postsynaptic ZI neurons and anxiety. We postulate that $LTP^{Pre}{}_{GLU}$ or $LTP^{Pre}{}_{GABA}$ in CN → ZI circuits may contribute to the maintenance of anxiety through synaptic-specific potentiation, providing a biophysical basis for brain function. A comparable phenomenon is only found at the hypothalamus-lateral habenula synapses, where stress experience activates both pre- and post-synaptic neurons and contributes to depression formation[34]. In particular, the plasticity of GABAergic transmission is currently understood to be primarily expressed postsynaptically, involving processes such as $GABA_AR$ decay or G-protein-coupled cascades[35,36]. Differently, the presynaptic form of plasticity at long-range GABAergic synapses uncovered in this study offers a cellular mechanism for not only synaptic information processing but also behavioral phenotypes.

Heterogeneous distribution of neuronal subtypes within the ZI and related behavior

Recently, there has been a significant focus on the diversity of ZI neurons and their association with various behavioral paradigms in rodents and non-human primates. Utilizing circuit-specific optogenetics and chemogenetics, multiple subsets of ZI neurons have been implicated in multiple innate behaviors[37–44]. In fact, the ZI demonstrates a rich diversity of neuronal subtypes and exhibits extensive connectivity with numerous brain regions. We find that CN projections are clustered in a narrow area in the ZI (bregma −2.00 to −2.80), which contains both excitatory and inhibitory neurons. The region receiving CN inputs differs from known ZI subregions, such as rostral ZI expressing GABA-positive neurons, dorsal ZI expressing neuronal nitric oxide synthase- and glutamate-positive neurons, ventral ZI expressing parvalbumin-positive neurons, and caudal ZI expressing glutamate-positive neurons[45–47].

It has been demonstrated that, in the ventral ZI, activating somatostatin-positive neurons induces anxiety, while activating calretinin-positive neurons or inhibiting glutamate-positive neurons alleviates anxiety[48], which is consistent with the present work. Furthermore, we have provided multiple lines of evidence showing that stimulating CN → ZI pathway has no effect on motor activity. While our study does not elucidate the mechanism by which ZI^{CN} neurons regulate anxiety, it is plausible that ZI^{CN} neurons may modulate anxiety by potentially influencing emotion-related brain regions, including the amygdala, given its central role in anxiety regulation and the close connections with the ZI[49].

The cerebellum is implicated in stress and anxiety through a variety of projections

Recent research has suggested a strong correlation between the cerebellum and stress, as well as anxiety, leading to the proposition that the cerebellum may be involved in stress-related disorders[50]. Previous research has demonstrated that DN neurons can be activated by chronic restraint stress[26], while our study has revealed that CN neurons are also responsive to various forms of acute stress, indicating their capacity to perceive stress stimuli. Here, we summarize that the cerebellum may participate in anxiety regulation through multiple pathways. First, both the cerebellum and vestibular system are potentially involved in emotional regulation[17], as the imbalance in individual homeostasis within this system leads to experiences of stress and subsequent anxiety and depression[51]. Second, the CN may exert direct or indirect influence on amygdala function through the thalamus[19,52], thereby modulating anxiety-related behavior. Finally, the excitatory projection from the CN to the VTA may be involved in the encoding of social behaviors and reward; bidirectional regulation of depression-like behaviors caused by chronic stress can be achieved through inhibition or activation of the DN → VTA projection[25,26]. Here, we demonstrate that either $CN^{GLU} \rightarrow ZI$ or $CN^{GABA} \rightarrow ZI$ circuit can play a crucial role in modulating anxiety-like behaviors through synaptic plasticity, and inhibiting the entire CN → ZI circuit leads to anxiety relief, suggesting that CN → ZI circuits under acute stress is to promote anxiety. These findings advance our understanding of the cerebellum's involvement in regulating mechanisms underlying stress and anxiety behaviors. Interestingly, the entire CN → ZI pathway and glutamatergic CN → amygdala pathway may regulate anxiety in opposite directions. As previous research suggests, inhibiting the CN → amygdala pathway reduces the level of anxiety alleviation induced by motor activity[19]. It should be noted that, in order to achieve similar modulatory effects, stronger optogenetic stimulations have been given to ZI^{GLU} neurons (Fig. 6) compared to ZI^{GABA} neurons (Fig. 4), which is consistent with less activity in $CN^{GABA} \rightarrow ZI^{GLU}$ pathway than in $CN^{GLU} \rightarrow ZI^{GABA}$ pathway (Fig. 3).

The cerebellar outputs may be a target for the treatment of affective disorders

It has been observed that patients with cerebellar damage exhibit symptoms such as anxiety, depression, and aggression[8]. Animal studies have also shown that mutations in SCA3 and SCA17, two subtypes of spinocerebellar ataxia, not only result in motor dysfunction but also give rise to a range of non-motor symptoms, with anxiety even manifesting prior to motor symptoms[53,54]. These symptoms involved in CCAS can be attributed to altered connectivity between the cerebellum and subcortical nuclei of the forebrain. We hypothesize that minor abnormalities in cerebello-cerebral connections may initiate an unexpected cascade of amplifying effects impacting brain homeostasis and resulting in psychiatric disorders. Considering the persistent interactions between the cerebellum and cerebral cortex throughout brain development[55], any adverse experience affecting a functioning cerebellum during childhood may cause structural and functional impairments to cerebellar outputs in adulthood, leading to mental abnormalities such as anxiety. It is notable that a vast number of cerebellar neurons control the activity of multiple brain regions through hierarchical amplifications of outputs. From this viewpoint, we propose that non-invasive stimulation targeting the cerebellum could potentially be utilized for treating CCAS in future clinical trials. Compared with DBS or non-invasive stimulations targeting the cerebral cortex, non-invasive stimulations, including transcranial magnetic stimulation and transcranial direct current stimulation, on the cerebellar cortex might bring considerable convenience and more potent stimulation effects to patients with affective disorders. In this regard, our current work offers another theoretical basis for future cerebellum-based non-invasive neural modulation.

Methods

Animals

All experiments were carried out in strict compliance with protocols approved by the Animal Care and Use Committee at Zhejiang University (ZJU) School of Medicine. C57BL/6J mice were obtained from

Table 1 | Virus names, injection sites, injection coordinates, injection volumes, and suppliers

Virus	Injection area	Injection coordinate	Injection volume	Company
AAV1-hSyn-Cre-EGFP	FN	ML: −0.74; AP: −6.30; DV: −3.25	100 nl	Taitool Biosci
AAV1-hSyn-Cre-EGFP	IN	ML: −1.45; AP: −6.24; DV: −3.32	100 nl	Taitool Biosci
AAV1-hSyn-Cre-EGFP	DN	ML: −2.15; AP: −6.12; DV: −3.42	100 nl	Taitool Biosci
AAV2/9-hSyn-FLEX-tdTomato	CN	ML −2.25; AP −6.20; DV −3.20	200 nl	Taitool Biosci
AAV2/9-CAG-FLEX-oChIEF-tdTomato	CN	ML −2.25; AP −6.20; DV −3.20	200 nl	Taitool Biosci
AAV2/2Retro-CAG-FLEX-Flpo	ZI	ML −1.45; AP −2.50; DV −3.95	200 nl	Taitool Biosci
AAV2/9-hEF1a-fDIO-GCaMP6m	CN	ML −2.25; AP −6.20; DV −3.20	300 nl	Taitool Biosci
AAV2/9-hSyn-FLEX-mGFP-2A-synaptophysin-mRuby	CN	ML −2.25; AP −6.20; DV −3.20	300 nl	Taitool Biosci
AAV2/9-hEF1a-DIO-eNpHR3.0-EYFP	CN	ML −2.25; AP −6.20; DV −3.20	300 nl	Taitool Biosci
AAV2/9-hEF1a-DIO-EYFP	CN	ML −2.25; AP −6.20; DV −3.20	300 nl	Taitool Biosci
AAV2/9-hEF1a-fDIO-hM3Dq-mCherry	CN	ML −2.25; AP −6.20; DV −3.20	300 nl	Taitool Biosci
AAV2/9-hEF1a-fDIO-hM4Di-mCherry	CN	ML −2.25; AP −6.20; DV −3.20	300 nl	Taitool Biosci
AAV2/9-hEF1a-fDIO-mCherry	CN	ML −2.25; AP −6.20; DV −3.20	300 nl	Taitool Biosci
AAV2/9-hEF1a-fDIO-mCherry-P2A-TetTox	CN	ML −2.25; AP −6.20; DV −3.20	250 nl	Taitool Biosci
AAV2/9-EF1a-DIO-TVA-EGFP AAV2/9-EF1a-DIO-oRG	ZI	ML −1.45; AP −2.50; DV −3.95	200 nl	BrainVTA Tech
RV-ENVA-ΔG-dsRed	ZI	ML −1.45; AP −2.50;DV −3.95	200 nl	BrainVTA Tech

the Laboratory Animal Center of Zhejiang Academy of Medical Sciences (Hangzhou, China). Original Ai9 (no. 007909), Ai14 (no. 007914), *vGat*-ires-Cre (no. 028862), and *vGluT2*-ires-Cre (no. 016963) were obtained from the Jackson Laboratory (Bar Harbor, ME). Mice were kept under temperature-controlled conditions on a 12:12 h light/dark cycle with food and water *ad libitum* at the animal facility at ZJU. All experiments were performed in age-matched male mice.

Viral injection and stereotaxic surgery

Mice were anesthetized with sodium pentobarbital (50 mg/kg, i.p.) and placed on a stereotaxic apparatus (RWD Life Tech, Shenzhen, China). A heating pad was used to maintain body temperature around 37 °C. After shaving the hair and incising the scalp, the connective tissue was gently removed with cotton swabs. Viruses were injected at a rate of 30 nl/min using a microinjector (R480, RWD Life Tech) and a micro pipette with a 10-μm tip. The viruses used in the present work are listed in Table 1 below. Both Taitool Biosci and BrainVTA Tech are located in Shanghai (China). The coordinates (unit: mm) were always determined according to the mouse brain atlas. Surgical sutures were used to close the skin after surgery. Mice were allowed to recover for 4 weeks before further experiments. After experiments, histological analysis was applied to verify the location of viral transduction. Data were excluded from analysis if viral transduction extended beyond the target region.

Antibodies

The antibody against GABA (#A2052; RRID: AB_477652) was from Sigma (St. Louis, MO). The antibody against SMI32 (#SMI-32R-100; RRID: AB_509997) was from Covance (Princeton, CT). Alexa Fluor-conjugated secondary antibodies, Goat anti-mouse Alexa Flour 488 (#A32723), Goat anti-rabbit Alexa Flour 488 (#A32721), and Goat anti-mouse Alexa Flour 647 (#A32733) were from Invitrogen (Carlsbad, CA).

Optogenetics

After three weeks of oChIEF or NpHR viral expression, optical fibers (200 μm O.D., 0.22 NA; Inper Tech, Hangzhou, China) were bilaterally positioned 200 μm above the ZI to enable in vivo optogenetic manipulation of CN → ZI axonal terminals. All fibers were secured to the skull with bone screws and dental cement. Mice were allowed a recovery period of at least 10 days after the implantation and habituated for 15 min after connecting to a laser source before behavioral tests were conducted. Laser at wavelengths of 473 nm (blue; 5 mW) or 589 nm (yellow; 10 mW) was applied and controlled using a programmed laser generator (B2-465; Inper Tech; for blue light) or (B2-589; Inper Tech). Laser intensity at the tip was calibrated with an optical power meter (UT385, Uni-Trend Tech, Dongguan, China).

Fiber photometry

Three weeks after viral injection, the mice were implanted with 200-μm diameter optical fibers for fiber photometry (Opt-fps-410/470; Inper Tech). The fibers were carefully positioned above the CN and secured to the skull surface using a thin layer of ultraviolet ray-cured dental cement. Subsequently, a second layer of dental cement was applied to firmly affix the fiber. To capture GCaMP6m fluorescent signals, a 470-nm light beam was emitted and reflected off a dichromic mirror, then focused by a 20× objective. In order to minimize bleaching, the intensity of the detecting laser at the tip of the fiber was adjusted to 20–40 μW/mm^2. The end of the fiber was imaged at a frame rate of 60 FPS and the mean value of an ROI was calculated using software from Inper Tech. Peak calcium transients were determined by averaging the values before and after the maximum value. Ca^{2+} traces and heat maps were plotted using Inper Plot software (Inper Tech).

General criteria for behavioral tests

The mice were extensively handled and acclimated to the test room for a minimum of 3 days prior to behavioral testing. Room temperature (RT) and humidity were maintained at stable levels throughout experiments, which were conducted during the daytime. Following a 4-week recovery period from viral injection, the mice underwent assessment in validated behavioral paradigms with specified duration and stimulation conditions. Upon completion of the experiment, all animals were euthanized for confirmation of virus expression using fluorescence imaging. Only data from animals with accurately placed optical fiber implants and virus expression were included in the analysis. For chemogenetics, animals were i.p. administered with CNO (Sigma, St. Louis, MO) (2 mg/kg) 25–30 min prior to the test.

Stress stimuli

Test mice were placed in a transparent chamber (30 cm × 30 cm × 30 cm) for 30 min, and then subjected to stress stimuli. Six paradigms were utilized in this study: neonatal mouse stress (pup stress), air puff stress (air puff), overhead object stress (overhead object), tail pinch stress (tail restraint), tail restraint stress (TRS), and social attack. 'pup

stress': newborn mice (P0-P1) were introduced into the chamber, and their behavior was observed. Three newborn mice were used for each trial with a 5-min interval. 'air puff': an ear-washing ball was directed towards the head of the mice for squeezing and blowing. Each mouse received five stimulations with an interval of 1–2 min. 'overhead object': a paper plane flew over the top of the mouse's head to simulate a natural predator. Each mouse was stimulated five times with an interval of 1–2 min. 'Tail pinch': the tail of each mouse was clamped with forceps for a total of 5 times per mouse, with a 2-min interval. 'TRS': The tail of each mouse was lifted, suspending the mouse before being released back down. This process was repeated five times, with a 2-min interval. 'social attack': an adult intruder mouse was introduced into the chamber, and its aggressive behavior towards the test mice was recorded for ~30 min.

ARS was performed according to previous work[30]. Four weeks after viral injection and fiber implantation, mice were immobilized in modified plastic syringes once for 2 h. Several holes were drilled in the ends of the syringes to allow the mice to breathe. ARS was conducted between 8:00 am and10:00 am, and behavioral tests were subsequently performed 0.5 h after the treatment.

Elevated plus maze (EPM)

The apparatus consists of two open arms (30 cm × 5 cm) and two closed arms (30 cm × 5 cm with walls 20 cm in height) intersecting at a central square (5 cm × 5 cm), positioned at a height of 50 cm from the ground. Mice were placed in the center, facing an open arm, and their behaviors were recorded over a period of 5 min. The time spent on the open arm and entries into the open arm were measured using Any-maze software (Stoelting, IL).

RTPP

The mice, which were implanted with optical fibers above the bilateral ZI, were placed in a custom-made arena (50 cm × 25 cm × 25 cm) consisting of two chambers for free movement. Their activity trajectory was recorded by a video camera positioned above the chamber and analyzed using Any-maze software. The experiment consisted of two phases: an initial test without light stimulation, where the mouse's time spent on each side was recorded, and a second phase with light stimulation, activating one side while leaving the other side unstimulated. The moving traces were analyzed using Any-maze.

CPP

The apparatus consists of three sections, comprising two main boxes (25 cm × 25 cm × 30 cm for each) and a buffer zone (20 cm × 15 cm × 30 cm). One box features a white background with black stripes on the wall and a metal plate with a round hole at the bottom. The other box has a black background with white stripes on the wall and is lined with metal cylinders at the bottom. The buffer zone's wall is gray. On day one, mice were placed in the center to freely explore the apparatus for 15 min. On day two, they were allowed to explore for another 15 min, and their time spent in each box was recorded as baseline to determine preference. Mice with a strong baseline preference for either side of the chamber (>70 %) were excluded. From day three to five, after installing baffles, mice were placed into the less preferred box (for *vGluT2*-Cre mice) or the more preferred box (for *vGat*-Cre mice) without light stimulation for 30 min. After 4-h rest, *vGluT2*-Cre mice were placed in the more preferred chamber paired with intracranial laser stimulation (470 nm, 20 Hz, 10 ms, 15 trains with 15-s interval); or *vGat*-Cre mice were place in the less preferred chamber paired with laser stimulation (470 nm, 20 Hz, 10 ms, 15 trains with 10-s interval). On day six, the baffles were opened and mice explored freely for 15 min. The activity time of mice in different chambers was recorded to assess their final preference for each chamber. The moving traces were analyzed using Any-maze.

Rotation and rearing test (RRT)

The mice were placed in a transparent resin cylinder (diameter 16 cm, height 25 cm) and monitored via video from above. Rearing times and net ipsilateral or contralateral rotations were scored. Rotations were defined as each 360° rotation that did not include a turn of >90° in the opposite direction. Rearing was defined as the body being raised with both forelimbs off the ground.

OFT

The mice were placed in a novel, brightly lit square plexiglass chamber measuring 50 cm × 50 cm × 50 cm (length × width × height). The activity of the mice was recorded and analyzed using Any-maze. During analysis, the arena was divided into two concentric zones named the inner zone (25 cm × 25 cm, length × width) and the outer zone. The travel parameters of the animals in each zone were recorded. In optogenetics experiments, the mice were allowed to freely explore for 5 min before light stimulation was administered. In chemogenetic experiments, the mice were injected with CNO and then observed for a period of 10 min starting from 30 min after injection. The moving traces were analyzed using Any-maze.

Rotarod test

To assess motor coordination, mice were tested on a rotating rod over two consecutive days. On the habituation day, the rotation velocity was set at 5 rpm. The mice underwent two training sessions, each lasting for 5 min with an inter-training interval of 1 h. On the test day, the initial rotation velocity was also set at 5 rpm but increased with a constant acceleration of 9 rpm/min, and the mice were tested for 5 min. The duration that mice stayed on the rod after it started to accelerate was recorded. To evaluate the effect of motor activity on anxiety, mice were trained twice a day with an interval of 8 h for four consecutive days. In each session, the rotation velocity increased at a constant acceleration of 9 rpm starting from 5 rpm. EPM test was conducted 30 min after rotarod running on the fourth day.

Artificial stimulation with optogenetics

The mice used in the study included *vGluT2*-Cre;Ai14 and *vGat*-Cre;Ai14 mice, both of which expressed oChIEF-tdtomato, as well as two control groups: Cre mice expressing tdtomato and Cre mice expressing oChIEF-tdtomato without light stimulation. After a 3-day acclimation period, the mice were placed in a chamber (30 cm × 30 cm × 30 cm) for 30 min each day, during which they had access to food and water. The training period lasted for 5 days (*vGluT2*-Cre) or 6 days (*vGat*-Cre), with daily light stimulation sessions (470 nm, 20 Hz, 10 ms, 15 trains with 15-s or 10-s interval) totaling 2 h, interspersed with 10-min intervals every 30 min. On day 6 or 7, trained mice underwent OFT for 10 min. On day 7 or 8, the rotarod test was conducted. On day 8 or 9, the EPM test was performed. Finally, on day 9 or 10, patch-clamp recordings were carried out in the ZI of the trained mice.

Cannula infusion

CNO was microinjected into the ZI using cannula implantation. A double dummy cannula that has a 0.5 mm extension beyond the end of the guide cannula with a metal cap was inserted into the guide cannula. Double injector cannulae were connected with a micro-syringe with a polyethylene pipe. The cannulae were left in the ZI for 4–5 min to allow adequate diffusion and minimize the spread of the drug. The infusion sites were checked after behavioral procedures, and only data from mice with correctly sited injections were used.

Histology and imaging

Mice were deeply anesthetized with sodium pentobarbital and perfused transcardially with phosphate buffer, followed by 4% paraformaldehyde in phosphate buffer. After the post-fixation overnight at

4 °C, brains were dehydrated with 30% sucrose. Continuous frozen coronal sections (20 μm) from the forebrain to the cerebellum were obtained using a cryostat microtome (Thermo Fisher, Waltham, MA) and placed sequentially in 96-well plates. For antibody fluorescence, sequential layers of the ZI and CN were transferred in blocking solution for 1 h at RT. After washing with PBS, sections were incubated with primary antibodies overnight at 4 °C. Primary antibody dilutions used for immunohistochemistry were 1:300 (GABA) and 1:1000 (SMI32). After rinses with PBS, sections were incubated with secondary antibodies (1:1000) for 2 h at RT, washed with PBS, and stained with DAPI. Immunohistochemical images were obtained with an A1R confocal microscope (Nikon, Tokyo). The parameters used in microscopy were consistent in all experiments.

Anatomic analysis

We acquired binary values for each image using the Threshold function of Fiji, and a baseline value was set based on five background pixels. The area with an intensity of at least 1.5-fold of the background value was determined as the actual injection fraction. For counting neurons, all slices were registered with the Allen Mouse Common Coordinate Framework (CCF) to normalize brain slices across investigated mice. In the coronal planes, labeled neurons were defined by the co-localization of tracer signal and DAPI at a fixed signal-to-noise ratio and counted using the Cell Counter and Analyze Particles functions of Fiji. To reconstruct labeled neurons in three-dimensional space, the coordinates of neurons were recorded after registering them using CCF, by which the animation showing 3D positions of neurons was constructed using Matlab or Rx64 4.0.0. To count neuronal numbers in the nuclei, the sections that contain target nuclei in the anterior-posterior direction were selected, and the representative shape of each nucleus was drawn in CorelDRAW software (Corel Inc.) according to the brain atlas.

Quality control of neuronal counting

Two investigators independently counted neurons for each slice section. The results showed that there was no difference between the two investigators for more than 90% of the counts. If there was a difference, we took the average of two counts as the final value. A confocal picture of one section and a vector graph of the registered brain map were imported into a file of CorelDRAW software. The picture and the map were overlapped to determine whether they belong to the same bregma level. Traced neurons were judged based on the staining color and shape. All these procedures were conducted using a large screen computer monitor for high resolution. All neurons within the ZI were counted.

Electrophysiology

All chemicals used in electrophysiology were from Sigma (St. Louis, MO). Mice were deeply anesthetized with isoflurane and quickly decapitated. Coronal slices of the ZI (250 μm) were prepared from anesthetic mice using a vibrating tissue slicer (VT1000S, Leica, Germany) and ice-cold standard artificial cerebrospinal fluid (aCSF) containing (in mM): 125 NaCl, 2.5 KCl, 1.25 NaH_2PO_4, 1 $MgCl_2$, 2 $CaCl_2$, 26 $NaHCO_3$ and 25 D-glucose, bubbled with 95% O_2/5% CO_2. After recovery for 30 min at 37 °C, slices were placed in a submerged chamber that was perfused at 2 ml/min with aCSF. Patch clamp electrodes (3–5 MΩ) were filled with an internal solution composed of (in mM) 134 K-gluconate, 6 KCl, 4 NaCl, 10 HEPES, 0.2 EGTA, 4 Na_2ATP, 0.3 Na_3GTP, and 14 Na_2phosphocreatine (pH 7.3, OSM 290).

Neurons were visualized under an upright microscope (BX51, Olympus) with a 40× water-immersion objective and equipped with infrared differential interference contrast enhancement. Fluorescent cells were visualized by illuminating with a mercury lamp. Whole-cell recordings were obtained with an Axon MultiClamp 700B amplifier (Molecular Devices, CA). Signals were digitized at 10 kHz and filtered at 3 kHz. Offline analysis was conducted using a sliding template algorithm (ClampFit 10, Molecular Devices). Current-clamp configuration was used to record neuronal firings, and voltage-clamp configuration was used to record photocurrents. Photostimulation (470 nm, 1-ms pulse) was delivered to evoke synaptic current using a laser generator (B2-465, Inper). TTX (1 μM) and 4AP (100 μM) were added into the external solution to verify monosynaptic responses. DNQX (10 μM) and AP5 (50 μM) were added to block glutamatergic current. GABAzine (10 μM) was added to block GABAergic current. For NpHR-expressing cells, photostimulation was delivered to ZI neurons using a laser generator (B2-589, Inper).

scRT-PCR

Cytoplasm from individual neurons was obtained from 10-min whole-cell recording, plus 1-min negative pressure applied by mouth. Harvested mRNA was first reverse-transcribed to cDNA using a Super Script III kit (Invitrogen), incubated at 50 °C for 50 min, and then terminated at 65 °C for 20 min. The entire cDNA was then amplified by multiplex PCR for 25 cycles, using QIAGEN Multiplex PCR Master Mix kit (Qiagen, Germany) in a volume of 100 μl. The transcripts of each tested gene were detected by a second round of PCR using an individual primer set: 1 μl of multiplex PCR mixture was applied as a template in a 10-μl reaction with HotStarTaq polymerase and cycled again (35 cycles). PCR products were run on a 2% agarose gel and visualized with ultraviolet light. The following oligonucleotide primers were used: for *vGluT2* (*Slc17a6*), *5′-TGT TCT GGC TTC TGG TGT CTT ACG AGA G-3′* sense and *5′-TTC CCG ACA GCG TGC CAA CA-3′* antisense (first round), and *5′-AGG TAC ATA GAA GAG AGC ATC GGG GAG A-3′* sense and *5′-CAC TGT AGT TGT TGA AAG AAT TTG CTT GCT C-3′* antisense (second round); for *vGat* (*Slc32a1*), *5′-ACT GCC ATA GGG GGA TTT GGT AGC-3′* sense and *5′-TGA TCT GGG CCA CAT TGA CC-3′* antisense (first round), and *5′-ATT CAG GGC ATG TTC GTG CT-3′* sense and *5′-ATG TGT GTC CAG TTC ATC AT-3′* antisense (second round). For *Gapdh, 5′-GGT GAA GGT CGG TGT GAA CG-3′* sense and *5′-CTC GCT CCT GGA AGA TGG TG-3′* antisense. TaqMan-GAPDH control reagent (Perkin Elmer, Waltham, MA) was used to amplify and detect *Gapdh*. The images of uncropped gel are presented in Supplementary Fig. 16.

LFP recording

The mouse scalp was incised to facilitate electrode implantation. During recording, mice were head-restrained using a custom-made pedestal. An optrode containing a 100-μm optic fiber was lowered into the ZI to simultaneously stimulate CN axons in the ZI and record LFP of ZI neurons. Signals were sampled by an amplifier (3600, A-M Systems) and an acquisition system (AD Instruments), digitized at 20 kHz, and acquired using PowerLab software. Light stimulation was produced by a laser generator connected to optrodes using patch cables. The laser intensity at the tip ranged from 1 mW to 5 mW, measured by an optical power meter.

Statistics

Experimenters who performed experiments and analyses were blinded to the genotypes until all data were integrated. No statistical methods were used to pre-determine sample sizes, which were based on our previous studies. Data were analyzed using Igor Pro 6.0 (Wavemetrics, Lake Oswego, OR), Graphpad Prism 8.0 (Graphad Software, San Diego, CA), SPSS 17.0 (IBM, Chicago, IL), MatLab, Rx64 4.0.0, Inper Plot (Inper), and Inper Code (Inper). All data sets were tested for the assumptions of normality of distribution. Statistical differences were determined using unpaired or paired two-sided Student's *t*-test for two-group comparisons, and one-way or two-way ANOVA followed by LSD's *post hoc* test for multiple comparisons. The level for significance was set at $p < 0.05$. "*n*" represents the number of animals or cells, depending on experiments. Data in the text and figures are presented as the mean ± SEM (standard error of the mean).

Reporting summary

Further information on research design is available in the Nature Portfolio Reporting Summary linked to this article.

Data availability

All relevant data supporting the present study have been provided in the main text, main figures, Supplementary Figs., and Supplementary Tables. Source data are provided with this paper Source data are provided with this paper.

Code availability

The fiber photometry data were analyzed using the commercial software packages Inper Plot and Inper Signal (Inper Tech).

References

1. Chrousos, G. P. Stress and disorders of the stress system. *Nat. Rev. Endocrinol.* **5**, 374–381 (2009).
2. Tovote, P., Fadok, J. P. & Lüthi, A. Neuronal circuits for fear and anxiety. *Nat. Rev. Neurosci.* **16**, 317–331 (2015).
3. Avery, S. N., Clauss, J. A. & Blackford, J. U. The human BNST: functional role in anxiety and addiction. *Neuropsychopharmacology* **41**, 126–141 (2016).
4. Gungor, N. Z. & Paré, D. Functional heterogeneity in the bed nucleus of the stria terminalis. *J. Neurosci.* **36**, 8038–8049 (2016).
5. Adhikari, A. Distributed circuits underlying anxiety. *Front Behav. Neurosci.* **8**, 112 (2014).
6. Schmahmann, J. D. & Sherman, J. C. The cerebellar cognitive affective syndrome. *Brain* **121**, 561–579 (1998).
7. Leggio, M. & Olivito, G. Topography of the cerebellum in relation to social brain regions and emotions. *Handb. Clin. Neurol.* **154**, 71–84 (2018).
8. Schmahmann, J. D., Weilburg, J. B. & Sherman, J. C. The neuropsychiatry of the cerebellum—insights from the clinic. *Cerebellum* **6**, 254–267 (2007).
9. Habas, C. et al. Distinct cerebellar contributions to intrinsic connectivity networks. *J. Neurosci.* **29**, 8586–8594 (2009).
10. O'Reilly, J. X., Beckmann, C. F., Tomassini, V., Ramnani, N. & Johansen-Berg, H. Distinct and overlapping functional zones in the cerebellum defined by resting state functional connectivity. *Cereb. Cortex* **20**, 953–965 (2010).
11. Ramnani, N. The primate cortico-cerebellar system: anatomy and function. *Nat. Rev. Neurosci.* **7**, 511–522 (2006).
12. Wang, S. S., Kloth, A. D. & Badura, A. The cerebellum, sensitive periods, and autism. *Neuron* **83**, 518–532 (2014).
13. Limperopoulos, C. et al. Injury to the premature cerebellum: outcome is related to remote cortical development. *Cereb. Cortex* **24**, 728–736 (2014).
14. Reeber, S. L., Otis, T. S. & Sillitoe, R. V. New roles for the cerebellum in health and disease. *Front Syst. Neurosci.* **7**, 83 (2013).
15. Hwang, K. D., Kim, S. J. & Lee, Y. S. Cerebellar circuits for classical fear conditioning. *Front Cell Neurosci.* **16**, 836948 (2022).
16. Zhu, J. N., Yung, W. H., Kwok-Chong Chow, B., Chan, Y. S. & Wang, J. J. The cerebellar-hypothalamic circuits: potential pathways underlying cerebellar involvement in somatic-visceral integration. *Brain Res Rev.* **52**, 93–106 (2006).
17. Brandt, T. & Dieterich, M. Excess anxiety' and 'less anxiety': both depend on vestibular function. *Curr. Opin. Neurol.* **33**, 136–141 (2020).
18. Jung, S. J. et al. Novel cerebello-amygdala connections provide missing link between cerebellum and limbic system. *Front Syst. Neurosci.* **16**, 879634 (2022).
19. Zhang, X. Y. et al. A role for the cerebellum in motor-triggered alleviation of anxiety. *Neuron* **112**, 1165–1181 (2024).
20. Yao, Q. et al. Effect of cerebellum stimulation on cognitive recovery in patients with Alzheimer disease: a randomized clinical trial. *Brain Stimul.* **15**, 910–920 (2022).
21. França, C., de Andrade, D. C., Teixeira, M. J. & Cury, R. G. Cerebellum as a possible target for neuromodulation after stroke. *Brain Stimul.* **11**, 1175–1176 (2018).
22. van Dun, K., Bodranghien, F., Manto, M. & Mariën, P. Targeting the cerebellum by noninvasive neurostimulation: a review. *Cerebellum* **16**, 695–741 (2017).
23. Kebschull, J. M. et al. Cerebellar nuclei evolved by repeatedly duplicating a conserved cell-type set. *Science* **370**, eabd5059 (2020).
24. Hoshino, M. et al. Ptf1a, a bHLH transcriptional gene, defines GABAergic neuronal fates in cerebellum. *Neuron* **47**, 201–213 (2005).
25. Carta, I. et al. Cerebellar modulation of the reward circuitry and social behavior. *Science* **363**, eaav0581 (2019).
26. Baek, S. J. et al. VTA-projecting cerebellar neurons mediate stress-dependent depression-like behaviors. *Elife* **11**, e72981 (2022).
27. Grillon, C. Startle reactivity and anxiety disorders: aversive conditioning, context, and neurobiology. *Biol. Psychiatry* **52**, 958–975 (2002).
28. Calhoon, G. G. & Tye, K. M. Resolving the neural circuits of anxiety. *Nat. Neurosci.* **18**, 1394–1404 (2015).
29. Zhou, L. et al. Celecoxib ameliorates seizure susceptibility in autosomal dominant lateral temporal epilepsy. *J. Neurosci.* **38**, 3346–3357 (2018).
30. Chen, D. et al. Microglia govern the extinction of acute stress-induced anxiety-like behaviors in male mice. *Nat. Commun.* **15**, 449 (2024).
31. Malik, R., Li, Y., Schamiloglu, S. & Sohal, V. S. Top–down control of hippocampal signal-to-noise by prefrontal long-range inhibition. *Cell* **185**, 1602–1617 (2022).
32. Melzer, S. & Monyer, H. Diversity and function of corticopetal and corticofugal GABAergic projection neurons. *Nat. Rev. Neurosci.* **21**, 499–515 (2020).
33. Llinàs, R., Precht, W. & Kitai, S. T. Cerebellar Purkinje cell projection to the peripheral vestibular organ in the frog. *Science* **158**, 1328–1330 (1967).
34. Zheng, Z. et al. Hypothalamus-habenula potentiation encodes chronic stress experience and drives depression onset. *Neuron* **110**, 1400–1415 (2022).
35. Xu, J. Y. & Sastry, B. R. Benzodiazepine involvement in LTP of the GABA-ergic IPSC in rat hippocampal CA1 neurons. *Brain Res.* **1062**, 134–143 (2005).
36. Nugent, F. S. & Kauer, J. A. LTP of GABAergic synapses in the ventral tegmental area and beyond. *J. Physiol.* **586**, 1487–1493 (2008).
37. Liu, K. et al. Lhx6-positive GABA-releasing neurons of the zona incerta promote sleep. *Nature* **548**, 582–587 (2017).
38. Zhang, X. & van den Pol, A. N. Rapid binge-like eating and body weight gain driven by zona incerta GABA neuron activation. *Science* **356**, 853–859 (2017).
39. Chou, X. L. et al. Inhibitory gain modulation of defense behaviors by zona incerta. *Nat. Commun.* **9**, 1151 (2018).
40. Venkataraman, A. et al. Modulation of fear generalization by the zona incerta. *Proc. Natl. Acad. Sci. USA* **116**, 9072–9077 (2019).
41. Wang, X. et al. A cross-modality enhancement of defensive flight via parvalbumin neurons in zona incerta. *Elife* **8**, e42728 (2019).
42. Shang, C. P. et al. A subcortical excitatory circuit for sensory-triggered predatory hunting in mice. *Nat. Neurosci.* **22**, 909–920 (2019).
43. Zhao, Z. D. et al. Zona incerta GABAergic neurons integrate prey-related sensory signals and induce an appetitive drive to promote hunting. *Nat. Neurosci.* **22**, 921–932 (2019).

44. Wang, H. et al. Incerta-thalamic circuit controls nocifensive behavior via cannabinoid type 1 receptors. *Neuron* **107**, 538–551 (2020).
45. Kolmac, C. & Mitrofanis, J. Distribution of various neurochemicals within the zona incerta: an immunocytochemical and histochemical study. *Anat. Embryol.* **199**, 265–280 (1999).
46. Watson, G. D., Smith, J. B. & Alloway, K. D. The zona incerta regulates communication between the superior colliculus and the posteromedial thalamus: Implications for thalamic interactions with the dorsolateral striatum. *J. Neurosci.* **35**, 9463–9476 (2015).
47. Li, L. X., Li, Y. L., Wu, J. T., Song, J. Z. & Li, X. M. Glutamatergic neurons in the caudal zona incerta regulate Parkinsonian motor symptoms in mice. *Neurosci. Bull.* **38**, 1–15 (2022).
48. Li, Z., Rizzi, G. & Tan, K. R. Zona incerta subpopulations differentially encode and modulate anxiety. *Sci. Adv.* **7**, eabf6709 (2021).
49. Yang, Y. et al. Whole-brain connectome of GABAergic neurons in the mouse zona incerta. *Neurosci. Bull.* **38**, 1315–1329 (2022).
50. Moreno-Rius, J. The cerebellum under stress. *Front Neuroendocrinol.* **54**, 100774 (2019).
51. Hilber, P. The role of the cerebellar and vestibular networks in anxiety disorders and depression: the internal model hypothesis. *Cerebellum* **21**, 791–800 (2022).
52. Frontera, J. L. et al. Bidirectional control of fear memories by cerebellar neurons projecting to the ventrolateral periaqueductal grey. *Nat. Commun.* **11**, 5207 (2020).
53. Kyriakou, E. I. et al. Anxiety and risk assessment-related traits in a rat model of Spinocerebellar ataxia type 17. *Behav. Brain Res.* **321**, 106–112 (2017).
54. Marinina, K. S., Bezprozvanny, I. B. & Egorova, P. A. Memory decline, anxiety and depression in the mouse model of spinocerebellar ataxia type 3. *Hum. Mol. Genet.* **33**, 299–317 (2024).
55. Tiemeier, H. et al. Cerebellum development during childhood and adolescence: a longitudinal morphometric MRI study. *Neuroimage* **49**, 63–70 (2010).

Acknowledgements

We thank members of the Shen lab for valuable comments and Dr. Sanhua Fang from the core facilities, Zhejiang University School of Medicine, for technical support. This work was supported by grants from the STI2030-Major Projects (2021ZD0204000, W.X. and Y.S.) and National Key R&D Program (2023YFE0206800, Y.S.) of the Ministry of Science and Technology of China, the National Natural Science Foundation of China (81625006, Y.S.; 31820103005, Y.S.; 32170976, L.Z.; 32225021, Y.G.; and 32200620, L.W.), Zhejiang Province Natural Science Foundation of China (LZ24C090003, Y.S. and LY21C090003, Z.L.), Guangzhou Medical Key Discipline Construction Project (2025-2027, J.L. and Y.S.), and the Peak Discipline Cultivation Program of Zhejiang University School of Basic Medicine (Y.G., L.W., and Y.S.).

Author contributions

Y.Z. and Y.S. designed the study; Y.Z., J.-T.W., J.-B.F., X.-Y.C., X.-T.W., L.W., and L.Z. performed the research. Y.Z., J.-T.W., J.-B.F., and X.-Y.C. analyzed the data. W.X., Y.G., J.L., and W.C. provided the reagents/analytic tools. Y.Z., J.L., W.C., L.Z., and Y.S. wrote the paper.

Competing interests

The authors declare no competing interests.

Additional information

Supplementary information The online version contains supplementary material available at https://doi.org/10.1038/s41467-025-58727-0.

Correspondence and requests for materials should be addressed to Jun Liu, Wei Chen, Lin Zhou or Ying Shen.

Peer review information *Nature Communications* thanks Avishek Adhikari and the other, anonymous, reviewer(s) for their contribution to the peer review of this work. A peer review file is available.